Astronomy & Astrophysics manuscript no. 40048corr
March 19, 2022

Evolution of the atomic component in protostellar outflows

T. Sperling[1], J. Eislöffel[1], C. Fischer[3], B. Nisini[2], T. Giannini[2], and A. Krabbe[3]

[1] Thüringer Landessternwarte, Sternwarte 5, D-07778, Tautenburg, Germany
[2] INAF—Osservatorio Astronomico di Roma, via Frascati 33, I-00040 Monte Porzio, Italy
[3] Deutsches SOFIA Institut University of Stuttgart, D-70569 Stuttgart, Germany

Received: 03 December 2020 / Accepted: 15 April 2021

ABSTRACT

Context. We present SOFIA/FIFI-LS observations of three Class 0 and one Class I outflows (Cep E, HH 1, HH 212, and L1551 IRS5) in the far-infrared $[O\,I]_{63\mu m}$ and $[O\,I]_{145\mu m}$ transitions. Spectroscopic $[O\,I]_{63\mu m}$ maps enabled us to infer the spatial extent of warm ($T \sim 500 - 1200$ K), low-excitation atomic gas within these protostellar outflows.
Aims. Our main goal is to determine mass-loss rates from the obtained $[OI]_{63\mu m}$ maps and compare these with accretion rates from other studies.
Methods. The far-infrared $[O\,I]_{63\mu m}$ emission line is predicted to be the main coolant of dense, dissociative J-shocks caused by decelerated wind or jet shocks. If proper shock conditions prevail, the instantaneous mass-ejection rate is directly connected to the $[O\,I]_{63\mu m}$ luminosity. In order to unravel evolutionary trends, we analysed a set of 14 Class 0/I outflow sources that were spatially resolved in the $[O\,I]_{63}$ emission. We compared these data with a sample of 72 Class 0/I/II outflow sources that have been observed with Herschel (WISH, DIGIT, WILL, GASPS surveys) without spatially resolving the $[O\,I]_{63\mu m}$ line.
Results. All our newly observed targets feature prominent $[O\,I]_{63\mu m}$ emission either close to the driving source (L1551 IRS5, HH 1, HH 212) or as extended jet-like or knotty emission region away from it (Cep E). The detected $[O\,I]_{63\mu m}$ emission can mostly be attributed to dissociative shocks and photodissociation regions (PDRs). Flux values at 63 μm and 145 μm of all four associated continuum sources are presented. We calculated mass-loss rates connected to the low-excitation, atomic outflow component in the range of $(5 - 50) \times 10^{-7}\,M_\odot\,\mathrm{yr}^{-1}$. Estimated ratios between the mass loss in the outflow and the mass accretion onto the source (jet efficiency ratios) are largely in the range of $\dot{M}_{\rm out}/\dot{M}_{\rm acc} \sim 0.05 - 0.5$ for the observed outflow sources, which are consistent with theoretical predictions and quoted Herschel data.
Conclusions. Our new observations and a comparison with the 72 outflow sources observed with Herschel indicate that the bulk ejected material in outflows from Class 0 sources resides in the molecular component, that is mass-loss rates derived from the $[O\,I]_{63}$ emission line significantly underestimate the total mass-loss rate during this and possibly also later phases of the star formation process.

Key words. Stars: formation, Stars: mass loss, ISM: jets and outflows, ISM: Herbig-Haro objects, ISM: individual objects: HH 212, HH 1, Cep E, L1551 IRS5

1. Introduction

Protostellar jets and outflows are spectacular astrophysical phenomena associated with star formation (Frank et al. 2014). Outflows from young stellar objects (YSOs) are nowadays commonly observed throughout the spectral range. Depending on the evolutionary status of the driving source, jets are mostly seen in distinctive molecular (e.g. SiO, CO, H_2), atomic (e.g. [O I]), or ionic (e.g. [Fe II], [S II], [N II]) transitions (Bally 2016), and until now only in a few cases in radio synchrotron emission (Vig et al. 2018; Anglada et al. 2018; Feeney-Johansson et al. 2019).
The broad categorisation of YSOs into Class 0, Class I, and Class II sources is well established (Lada 1987; Andre et al. 1993; Greene et al. 1994), and in this context it may seem reasonable that a comparable evolutionary scheme for their connected outflows can be sought out as well.
This idea has been tackled by a handful of studies (e.g. Ellerbroek et al. 2013; Watson et al. 2016; Mottram et al. 2017) mainly focusing on evolutionary indicators such as the efficiency ratio $f := \dot{M}_{\rm out}/\dot{M}_{\rm acc}$ of the protostar-outflow system. Here, $\dot{M}_{\rm out}$ and $\dot{M}_{\rm acc}$ represent the mass-ejection rate and the mass-accretion rate, respectively. Watson et al. (2016) claimed to have identified a trend of decreasing mass loss among Class 0, Class I, and Class II sources. Reasonable doubts for this hypothesis are articulated in Mottram et al. (2017), who identified different observing strategies as responsible for that finding. However, the determination of mass-ejection rates in all mentioned studies have to be reviewed since the outflow regions were observed with a poor spatial resolution. Furthermore, outflow rates, which are usually calculated from the far-infrared $[O\,I]_{63}$ line luminosity, can be meaningless if proper shock conditions of the underlying Hollenbach & McKee (1989) shock model do not prevail (Hartigan et al. 2019; Sperling et al. 2020).
In their survey, Alonso-Martínez et al. (2017) detected the $[O\,I]_{63}$ emission line towards all young outflow sources (Classes I, II, and III), supporting the notion that the $[O\,I]_{63}$ emission line traces the warm ($T \sim 500 - 1500$ K), shock-excited gas component in protostellar outflows. In addition, the $[O\,I]_{63}$ emission line is expected to be comparably bright among other emission lines in low-excitation atomic jets, making it a reasonable basis for observational studies of protostellar outflows.
Only a handful protostellar outflows have been observed spatially resolving the far-infrared $[O\,I]_{63}$ emission line (Podio et al. 2012; Nisini et al. 2015; Dionatos & Güdel 2017; Sperling et al. 2020). A detailed analysis of these targets mostly supports the

Table 1: Target information.

Source	Class	Cloud	R.A. (J2000)[a]	Decl. (J2000)[a]	D[b]	$L_{\rm bol}$[c]	P.A.[h]
			(h m s)	(° ′ ″)	(pc)	($L_\odot$)	(°)
IRAS 23011+6126 (Cep E)	0[g]	Cepheus, OB3	23 03 12.8	+61 42 26	730	~ 75[d]	25
VLA 1 (HH 1)	0[f]	Orion A, L1641	05 36 22.8	−06 46 06	430	~ 46[d]	145
IRAS 05413-0104 (HH 212)	0[g]	Orion B, L1630	05 43 51.4	−01 02 53	420	~ 13[d]	30
L1551 IRS 5	I[g]	Taurus, L1551	04 31 34.2	+18 08 05	140	~ 23[e]	75

Notes. [(a)] Taken from the Two Micron All Sky Survey (2MASS). [(b)] Rounded from Zucker et al. (2019) based on GAIA DR2, except Cep E taken from Kun et al. (2008). [(c)] We corrected the luminosities taken from the cited papers for our assumed distances: $L_{\rm bol} = (D_{\rm adopted}/D_{\rm paper})^2 L_{\rm bol}^{\rm paper}$. [(d)] van Dishoeck et al. (2011). [(e)] Karska et al. (2018). [(f)] AMI Consortium et al. (2012); Chini et al. (2001). [(g)] Froebrich (2005). [(h)] Position angle of the outflow.

notion of the shock origin of the detected [O I]$_{63}$ emission. In addition, specific line ratios observed towards protostellar outflows can help to rule out other possible [O I]$_{63}$ origins such as photodissociation regions (PDRs) or a disc (e.g. Watson et al. 2016).

In this context, we present new SOFIA/FIFI-LS observations of four Class 0/I outflow sources (Cep E, L1551 IRS5, HH 212, HH 1, see Table 1) spatially resolving [O I]$_{63,145}$ along their outflow regions close to their respective driving sources. These maps enable us to measure the instantaneous mass-loss rates residing in the outflows. Together with accretion rates estimated from bolometric luminosities (Gullbring et al. 1998; Hartmann et al. 1998; White & Hillenbrand 2004), our main intention is to revisit the prominence of the atomic flow component at different evolutionary stages of the driving source.

2. Observations

The observations were obtained with the FIFI-LS instrument (Looney et al. 2000; Fischer et al. 2018; Colditz et al. 2018) aboard the flying observatory SOFIA (Young et al. 2012). SOFIA is a modified Boeing 747SP aircraft equipped with a 2.5 m effective diameter reflecting telescope. The FIFI-LS instrument is an integral field, far-infrared spectrometer consisting of two independent grating spectrometers simultaneously operating at 51-120 µm (blue channel) and 115-200 µm (red channel). Both channels are composed of a 5×5 pixel array with a field of view of $30'' \times 30''$ in the blue channel and $1' \times 1'$ in the red channel. All four targets were mapped along their outflow axis close to their respective driving sources in the [O I] 63.1837 µm and [O I] 145.5254 µm far-infrared fine structure lines[1]. The diffraction-limited full width at half maximum (FWHM) beam sizes are 5.″4 at 63 µm and 12.″4 at 145 µm. The spectral resolutions $R = \lambda/\Delta\lambda$ are specified as 1300 (63 µm) and 1000 (145 µm), which corresponds to a medium velocity resolution of 231 km s^{-1} and 300 km s^{-1}. The data were acquired in observing Cycle 7 (programme IDs: 03_0073, 07_0069) in two-point symmetric chop mode.

3. Data reduction

We applied the same data reduction technique as described in detail in Sperling et al. (2020), which can be briefly summarised as follows. According to the flight parameters (i.e. the flight altitude H, the zenith angle θ, and water vapour overburden wvp), we specified a suitable synthetic transmission model $\tau(\lambda, H, \theta, wvp)$ for the atmosphere (ATRAN model, Lord 1992). The expected continuum emission together with a potentially present emission line is modelled as a four-parametric 1D-Gaussian function $\varphi(\lambda; A, \sigma, \mu, B)$. Thus, for each spatial pixel (also called spaxel) in our obtained data cubes, a non-linear least-squares fit to the function,

$$y = \left[\varphi(\lambda; A, \sigma, \mu, B) \cdot \tau(\lambda, H, \theta, wvp)\right] * \mathrm{SIF}\,(\lambda; R)\,, \quad (1)$$

is performed to extract the continuum as well as the continuum-subtracted line information in each spaxel (Figs. 1–4). In Eq. 1, the FIFI-LS spectral instrument function depending on the spectral resolution R is denoted as SIF $(\lambda; R)$.

Table 2 lists the selected ATRAN parameters for our four targets. Water vapour values therein represent actual measurements during observations (Fischer et al. in prep.). We estimate the uncertainties introduced by the time-averaged atmospheric modelling to be not more than 5 %. The total uncertainty in the absolute flux calibration for the integrated line fluxes amounts to approximately 20 %.

The observed [O I]$_{63}$ line widths ($\Delta v^2_{\rm obs} = \Delta v^2_{\rm line} + \Delta v^2_{\rm FIFI}$) are of the order of 250−350 km s^{-1}, indicating that the line is spectrally unresolved. We therefore constrain the intrinsic line width in our data reduction pipeline to be in the range of $50 - 300$ km s^{-1}.

Table 2: SOFIA flight information and chosen ATRAN parameters for the five observed targets (zenith angle θ, flight altitude H, water vapour overburden wvp).

Object	Obs. date	Flight	Time[a]	θ	H	wvp
			(min)	(°)	(kft)	(µm)
Cep E	2019-10-30	631	52	50	44	4.00
VLA 1, HH 1	2018-11-09	527	84	45	43	4.00
HH 212	2018-11-08	526	49	40	43	4.25
L1551IRS5	2019-11-07	637	21	45	43	4.50

Notes. [(a)] Total effective on-source integration time.

4. Results

4.1. Continuum sources

The obtained continuum maps of HH 1, HH 212, Cep E, and L1551 are presented in Appendix A (Fig. 8). With regard to Cep E, the continuum source IRAS 23 011+6126 (also Cep E-mm, Lefloch et al. 1996; Chini et al. 2001), which drives the

[1] https://www.mpe.mpg.de/ir/ISO/linelists/FSlines.html

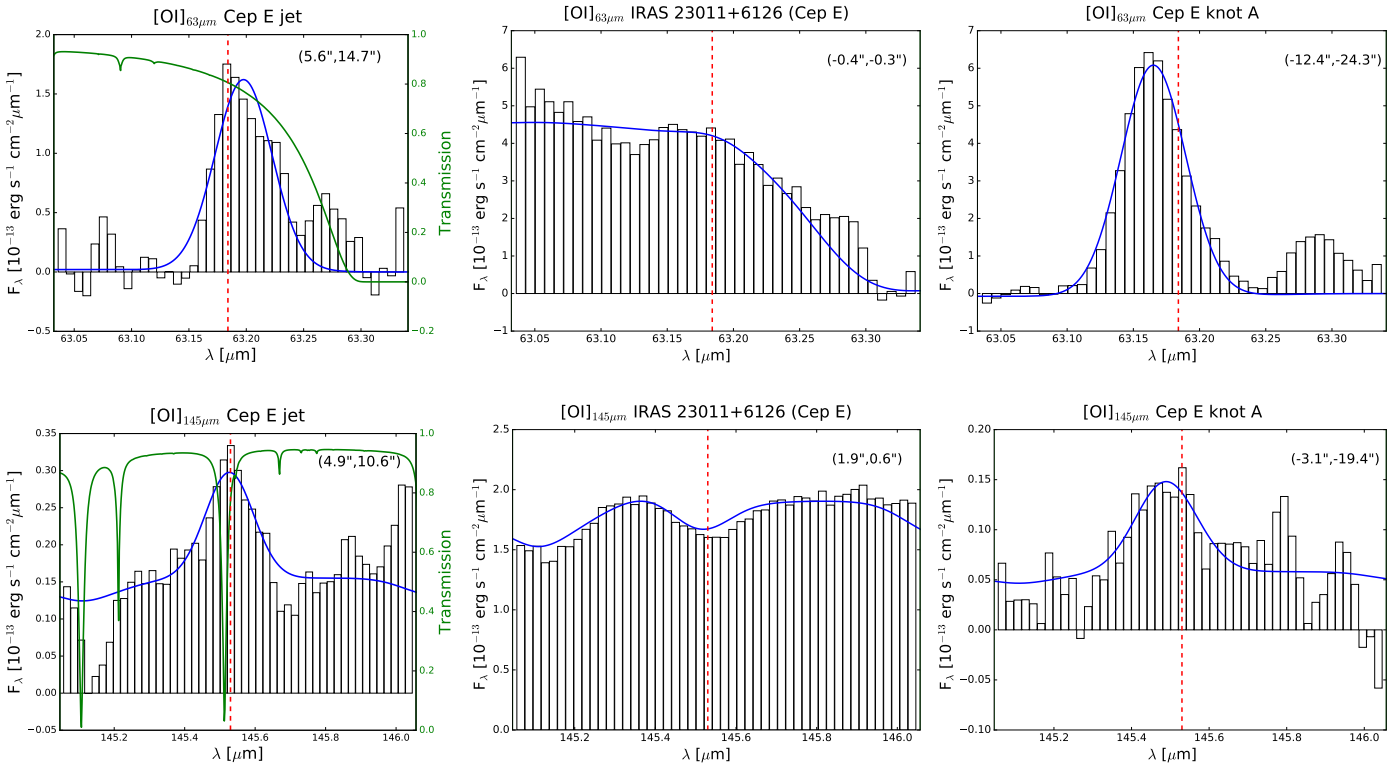

Fig. 1: Sample spectra of the detected [O I]$_{63,145}$ lines at different regions of Cep E. Green lines display the atmospheric transmission τ in the spectral regions around both relevant far-infrared [O I] transitions. The fitted model function y (Eq. 1) is plotted as a blue line in each spaxel. Vertical dashed red lines mark the position of the rest wavelengths of the [O I]$_{63,145}$ emission lines. Numbers in parentheses in the upper right corner indicate the individual spaxel position with respect to the driving source (see Fig. 5), that is the offset in right ascension and declination in units of arcseconds (ΔRA[″], ΔDEC[″]).

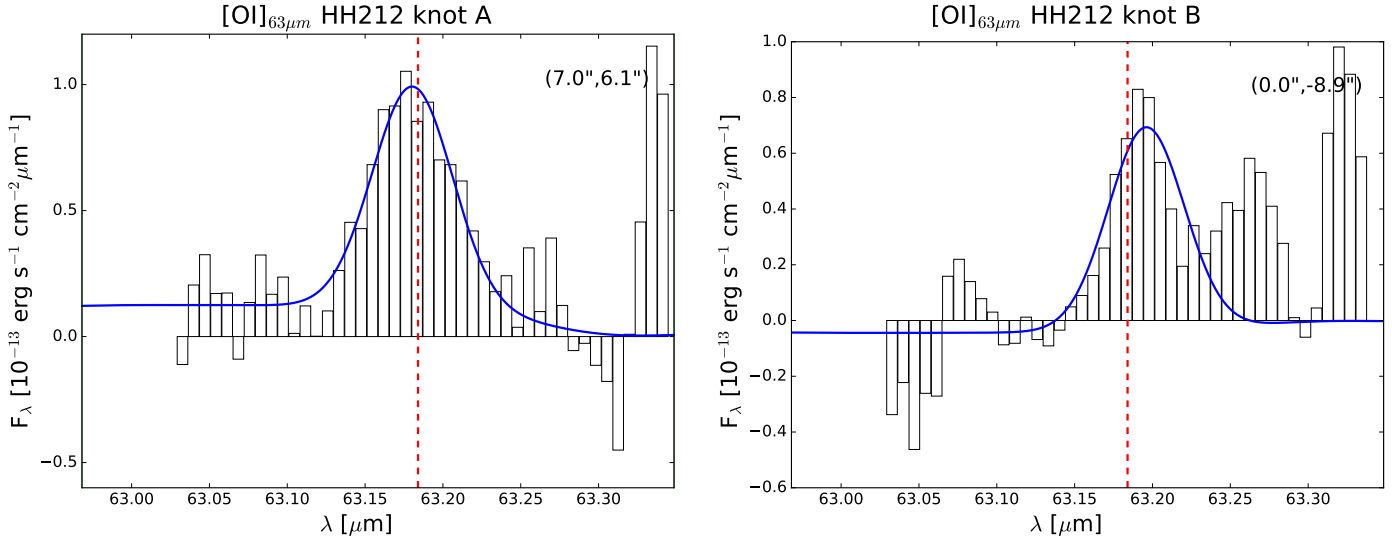

Fig. 2: Same as in Figure 1, but for HH 212.

powerful Cep E outflow (e.g. Eislöffel et al. 1996; Ayala et al. 2000; Lefloch et al. 2015), is detected in both FIFI-LS channels. Millimetre observations indicate that IRAS 23011+6126 is a system of two protostars (separation $\sim 2''$), namely Cep E-A and Cep E-B (Ospina-Zamudio et al. 2018), which appear as one continuum source in our maps. After subtracting this continuum source, a possible second source becomes visible at location $(\alpha, \delta)_{J2000}$ =($23^h03^m08\overset{s}{.}7$, $61°42'\ 38\overset{''}{.}0$) at 145 µm.

The HH 1/2 complex is among the brightest HH objects in the sky and has been studied extensively (e.g. see review in Raga et al. 2011). A central source at the location of VLA 1 (Pravdo et al. 1985; Rodríguez et al. 2000) is detected prominently in the red channel but very faintly in the blue channel. Inbetween

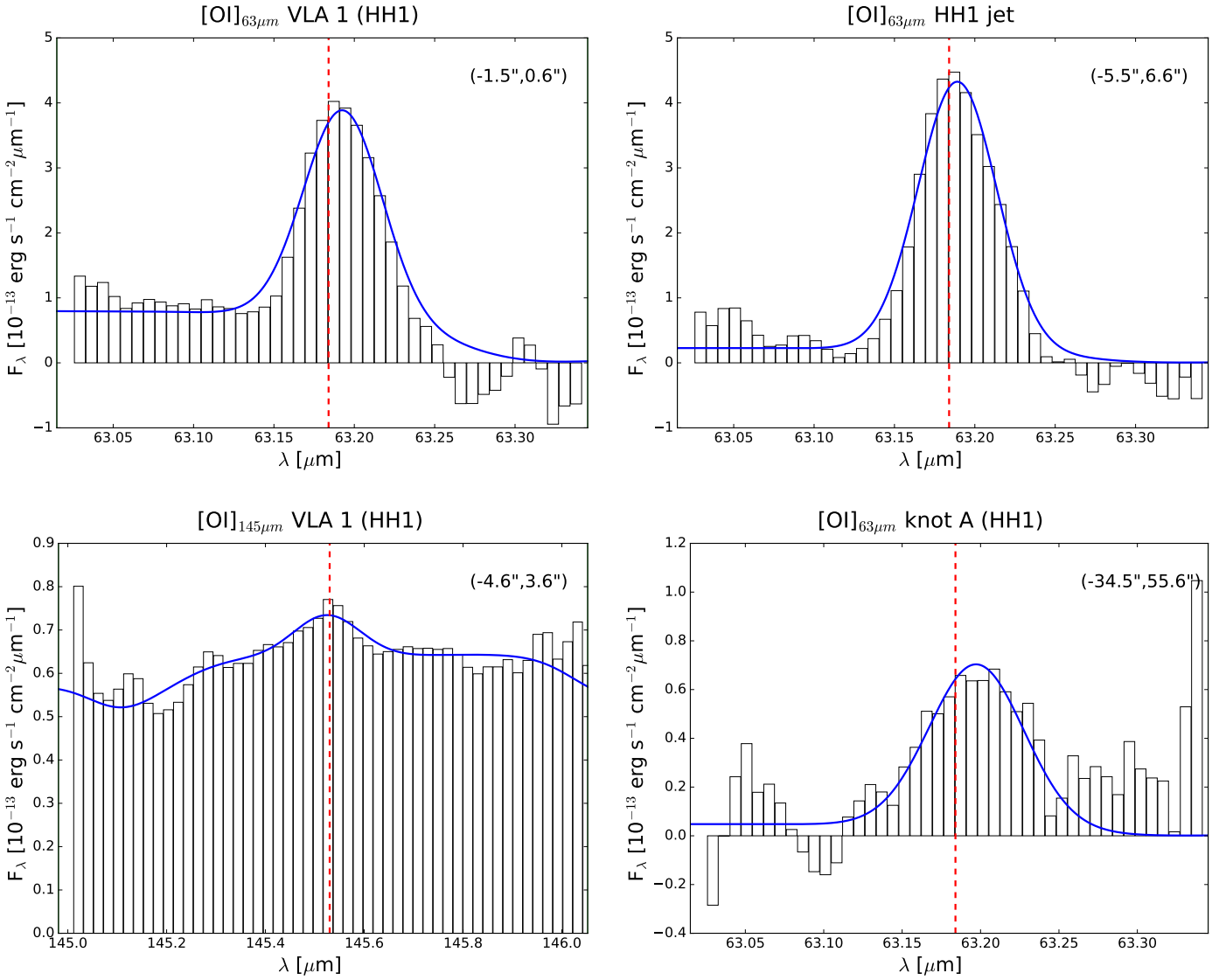

Fig. 3: Same as in Figure 1, but for HH 1.

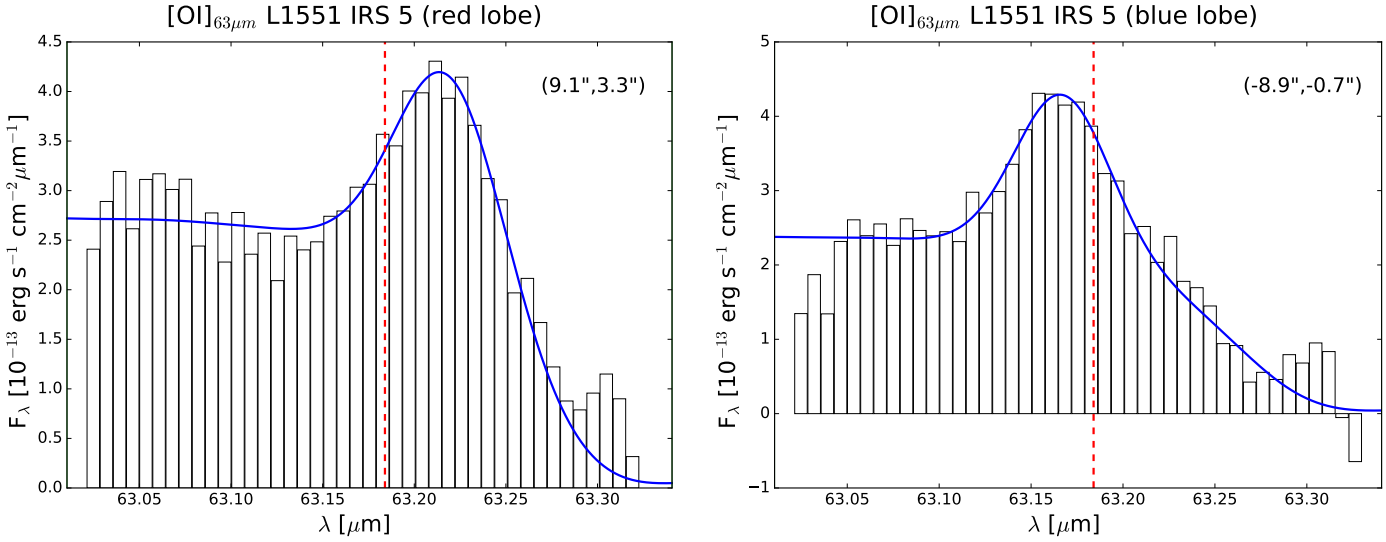

Fig. 4: Same as in Figure 1, but for L1551.

Table 3: Measured background-corrected continuum fluxes of our objects (flux in units: 10^{-13} erg s^{-1} cm^{-2} μm^{-1}).

Obj.	$F_{63\mu m} \pm \Delta F_{63\mu m}$	$F_{145\mu m} \pm \Delta F_{145\mu m}$
Cep E	361.4 ± 9.4	170.3 ± 1.7
HH 1	127.7 ± 14.1	117.8 ± 1.1
HH 1 radio source	–	223.2 ± 3.0[a]
HH 212	95.3 ± 8.3	81.3 ± 1.5
L1551	1857.7 ± 24.5	572.4 ± 7.0

Notes. [(a)] The detected radio source is located at the edge of the obtained continuum map and thus no aperture photometry could be done. The stated value is the integrated flux within the aperture of $1.5\,\sigma_s$ of the fitted 2D Gaussian.

the HH 1 jet and the bow-shock region HH 1 lies the unrelated Cohen-Schwartz star (Cohen & Schwartz 1979), which is not seen in our maps. In the red channel, the known radio source is detected at $(\alpha, \delta)_{J2000}$ =($5^h36^m18\overset{s}{.}9$, −06°45′26″), Pravdo et al. (1985).

The HH 212 outflow in L1630 in Orion is driven by a Class 0 protostar IRAS 05413–0104 (Froebrich 2005). We detect one continuum source in the 63 μm and 145 μm maps located at $(\alpha, \delta)_{J2000}$ =($5^h43^m51\overset{s}{.}2$, −1°02′ 56″.2) and $(\alpha, \delta)_{J2000}$ =($5^h43^m51\overset{s}{.}3$, −1°02′ 53″.8), respectively; hence, their declinations differ by about 2″.5. However, since the mentioned offset is within the accuracy of the SOFIA positions, we identify both detected sources as the HH 212 driving source IRAS 05413–0104. The refined coordinates of the associated VLA source (Galván-Madrid et al. 2004; Codella et al. 2007) are more in line with the position of the detected 145 μm source. Additionally, Chen et al. (2013) detected three close by continuum sources (HH 212 MMS1, MMS2, MMS3) at IRAS 05413–0104. This triple system is not resolved in our maps, since their mutual separation is smaller than 1″. About 7″ away from IRAS 05413–0104, a further source was detected in the near- and mid-infrared by Reipurth et al. (2019): IRS-B, which is located at $(\alpha, \delta)_{J2000}$ = ($05^h43^m51\overset{s}{.}2$, −01°02′47″). This source is not detected in our continuum and [O I] maps.

In the dark molecular cloud L1551, the infrared source IRS5 (Strom et al. 1976) drives powerful bipolar outflows that are associated with various Herbig-Haro objects (e.g. Fridlund & Liseau 1994; Devine et al. 1999; Hayashi & Pyo 2009). We detect a continuum source in both channels. Its coordinates are in agreement with the location of IRS 5 (Bally et al. 2003). L1551 IRS5 is a protostellar binary system with a separation of only ∼ 0″.3 (e.g. Bieging & Cohen 1985; Looney et al. 1997; Rodríguez et al. 1986, 1998, 2003). Tentatively, a third source was detected by Lim & Takakuwa (2006). At the given spatial resolution in our maps, the sources appear as one continuum source.

We fitted a 2D Gaussian to the detected continuum sources to measure the continuum flux within a circular aperture of radius $1.5\,\sigma_{Gauss}$ (Mighell 1999). In the case of the well-known radio source located at the edge of the 145 μm map of HH 1, this method could not be applied since parts of the source lie outside the map, and therefore the aperture covers a region of unspecified continuum pixels. Instead, we analytically integrated the fitted 2D Gaussian within an aperture of radius $1.5\,\sigma_{Gauss}$ to estimate the continuum flux. All continuum fluxes are reported in Table 3. The listed values are in line with expected values from the SIMBAD database.

The observed FWHM of the continuum sources are 10 – 13″ in the blue channel and 20 – 22″ in the red channel. We therefore conclude that all observed sources are extended.

4.2. [O I] Morphology and line fluxes

In this section, we briefly describe the morphology of the obtained $[O\,I]_{63}$ maps of the observed targets (Fig. 5). The $[O\,I]_{145}$ is not presented here since the $[O\,I]_{145}$ line was detected only in a few regions at low signal-to-noise. A detailed analysis of the detected $[O\,I]_{63}$ emission and schematic views are presented in the Appendix.

The continuum-subtracted $[O\,I]_{63}$ map of Cep E reveals a bright and extended $[O\,I]_{63}$ emission knot A located about 20″ south of the continuum source IRAS 23011+6126. Adopting the knot denotation from Gómez-Ruiz et al. (2012), for example, we find that this emission region coincides with the blueshifted lobe, BII, and partly with BI. On the opposite side to knot A in a north-easterly direction, a prominent 35″ long jet-like structure is detected. This emission region matches with the location of the redshifted lobes RII and RI fairly well (Gusdorf et al. 2017). We note that the emission region at RI and RII is slightly curved towards the eastern direction, meaning in the opposite direction to that one would expect to see from H_2 observations presented in Eislöffel et al. (1996). At the location of IRAS 23011+6126 no significant $[O\,I]_{63}$ emission is detected. The $[O\,I]_{145}$ line is detected at the Cep E jet and knot A in only a few spaxels.

The HH 1 jet (e.g. Eislöffel et al. 1994; Hester et al. 1998) is prominently seen in $[O\,I]_{63}$ and features one bright emission knot about 5″ north-west of VLA 1. Yellow crosses mark the positions of the prominent optical knots (Bally et al. 2002). We also detect strong $[O\,I]_{63}$ emission at the driving source VLA 1 and faint $[O\,I]_{63}$ emission about 65″ away from VLA 1 at HH 1. No $[O\,I]_{63}$ is detected at the location of the C-S-star. The $[O\,I]_{145}$ is detected in only a few spaxels at VLA 1 and the HH 1 jet.

Serving as orientation, we mark the positions of the knots seen in H_2 as yellow crosses (Zinnecker et al. 1998). Two bright $[O\,I]_{63}$ emission regions (knot A and B) are located opposite each other with IRAS 05413–0104 roughly in the middle, and together they portray a symmetric constellation. The emission knot A is brighter and more extended than knot B. Both knots and the continuum source lie on a projected line at P.A. ∼ 25°. Since the astrometry is only accurate to a few arcseconds and the HH 212 jet reflects a remarkably high symmetry, we conclude that the $[O\,I]_{63}$ emission of the northern knot A coincides with NK1 and the southern knot B with SK1. No significant $[O\,I]_{63}$ emission is detected along the jet axis towards SK7 and SB1/2.

In the $[O\,I]_{145}$ map, a very bright emission knot C is present a few arcseconds downstream of SB1/2 (see Fig. 9 and Fig. 10 in the Appendix). Unfortunately, this region is at the edge of the $[O\,I]_{63}$ map and thus not seen there.

We record bright $[O\,I]_{63}$ emission at the detected continuum source. The peak of this extended, blob-like emission is located a few arcseconds from the source position. The [O I] emission region appears to be stretched out alongside an axis at P.A. ∼ 250°. This position angle is consistent with the jet directions of the northern and southern jets seen in [Fe II] (Pyo et al. 2009) or H_2 (Davis et al. 2002). Serving as orientation, we marked the position of the distinctive [Fe II] emission knots PHK2 and PHK3, as well as the brightest parts of the northern and southern jets (Pyo et al. 2002). The innermost parts of the two marked jets emerging from IRS5 roughly match with the brightest [O I] emission region. At PHK3, almost no [O I] emission is detected. North-east of the source, the observed $[O\,I]_{63}$ line is redshifted, and to-

Table 4: Relevant information on the aperture boxes, which are sketched in the continuum-subtracted $[O\,I]_{63}$ emission maps (Fig. 5). Fluxes measured within these boxes are listed in units of 10^{-13} erg s^{-1} cm^{-2}.

			$[O\,I]_{63\mu m}$		$[O\,I]_{145\mu m}$	
Obj.	Region	Size	$F_{63\mu m}$	$L([O\,I]_{63})/L_\odot$	$F_{145\mu m}$	$[O\,I]_{63}$ origin (see Appendix)
Cep E	knot A	25″× 23″	78.38 ± 3.69	$13.06 \pm 0.62 \times 10^{-2}$	$< 7.1^a$	PDR + partly dissociative J-shocks
	jet	35″× 23″	55.99 ± 3.43	$9.33 \pm 0.57 \times 10^{-2}$	2.39 ± 0.82	PDR + a few internal shocks (mostly non-dissociative)
HH 1	VLA 1	50″× 25″	97.50 ± 2.59	$5.63 \pm 0.15 \times 10^{-2}$	$< 56.3^a$	PDR + dissociative J-shocks
	knot A	20″× 20″	10.74 ± 1.79	$6.21 \pm 1.04 \times 10^{-3}$	$< 3.0^a$	PDR + cooling zone behind bow shocks
HH 212	knot A and B	30″× 15″	17.90 ± 3.47	$9.87 \pm 1.92 \times 10^{-3}$	$< 6.6^a$	dissociative J-shocks
L1551	IRS 5	25″× 18″	83.70 ± 4.52	$5.13 \pm 0.28 \times 10^{-3}$	$< 18.7^a$	dissociative J-shocks, disc winds, and deflections

Notes. [a] The listed value corresponds to the 3 σ upper limit.

Table 5: Mass-loss rates of the observed targets. Column 5: Derived from jet geometry (i.e. Eq. 2). Column 6: Derived from the Hollenbach & McKee (1989) shock model, that is Eq. 3. Column 7: Mass-loss rates from the literature that are connected to other outflow components, meaning they are traced by species other than [O I] as indicated. Mass accretion rates in Column 8 are calculated from Eq. 4 unless stated otherwise.

Obj.	Region	θ	v_t	$\dot{M}_{out}^{lum}([O\,I])$	$\dot{M}_{out}^{shock}([O\,I])$	$\dot{M}_{out}^{other}$ & component	$\dot{M}_{acc}$ [e]
		(″)	(km s^{-1})	(10^{-7} $M_\odot$ yr^{-1})	(10^{-7} $M_\odot$ yr^{-1})	(10^{-7} $M_\odot$ yr^{-1})	(10^{-7} $M_\odot$ yr^{-1})
Cep E	knot A	25	95[a]	$\lesssim 22.4 - 45.5$	$\lesssim 124.4 - 136.7$	~ 200[j] & CO	170[f]
	jet	35	60[a]	$\lesssim 7.2 - 14.7$	$\lesssim 87.5 - 99.0$		
HH 1	VLA 1	50	300[b]	$\lesssim 25.9 - 52.6$	$\lesssim 54.9 - 57.8$	~ 6[k] & [Fe II]	290[g]
	knot A	20	400[b]	$\lesssim 9.5 - 19.4$	$\lesssim 5.2 - 7.2$	~ 4[k] & [S II]	
						~ 0.1[k] & H_2	
						~ 15[l] & CO	
HH 212	knots A and B	30	150[c]	3.9 – 7.9	8.0 – 11.8	~ 10[m] & CO, SO, SiO	80[h]
						≤ 3[n] & CO, SiO	
						~ 1[o] & H_2	
L1551	IRS 5	25	120[d]	5.8 – 11.8	4.9 – 5.4	$\gtrsim 100$[p] & CO, HCO^+, swept-up gas	30[i]
						~ 8.6[q] & HI	
						~ 1.7[r] & [Fe II]	
						~ 0.4[r] & H_2	

Notes. [a] Proper motions from Noriega-Crespo et al. (2014). [b] Proper motions from Bally et al. (2002). [c] Proper motions from Noriega-Crespo et al. (2020). [d] Proper motions from Fridlund & Liseau (1994). [e] Calculated from their bolometric luminosities (see Section 4.4). [f] Our estimate (see Section 4.4). From SED modeling, Velusamy et al. (2011) estimated a surprisingly high accretion rate for Cep E-mm of the order of $10^{-4} M_\odot$ yr^{-1}. [g] The stated value is in good agreement with Fischer et al. (2010). Therein, the source of the HH 1-2 outflow is labelled HOPS 203. [h] The stated value is in good agreement with Lee et al. (2014). [i] The stated value is in good agreement with, for example, Osorio et al. (2003), Liseau et al. (2005), and Gramajo et al. (2007). [j] Lefloch et al. (2015): This material is directly connected to the Cep E jet and not to swept-up gas. [k] Nisini et al. (2005). [l] From CO J=1–0 observations undertaken by Tanabe et al. (2019), it is unclear if it is entrained material or not. [m] Lee et al. (2007a); Podio et al. (2015); Lee et al. (2015); Lee (2020). [n] Cabrit et al. (2012). [o] Davis et al. (2000). [p] Hogerheijde et al. (1998); Fridlund et al. (2002); Yıldız et al. (2015). [q] Giovanardi et al. (2000). [r] Davis et al. (2003).

wards south-west, the line is blueshifted (see Fig. 4). Thus, both lobes of the outflow are prominently detected in [O I].

We determined [O I] line fluxes for all relevant outflow regions (green boxes in Fig. 5) using the same method presented in Sperling et al. (2020). Measured [O I] line fluxes and luminosities are listed in Table 4. We consider the impact of foreground absorption by cold gas in the line of sight to be negligible (see discussion in Nisini et al. 2015).

4.3. Mass-loss rates

We wish to estimate mass-loss rates from the obtained $[O\,I]_{63}$ maps of the observed outflows. Basically, two distinct physical approaches are worth considering here: a) $\dot{M}_{out}$ from the jet luminosity; b) $\dot{M}_{out}$ from a shock model. As described in detail in the corresponding Sections, 4.3.1 and 4.3.2, both methods are based on different model assumptions. Common to both is the underlying premise that any PDR (Goldsmith 2019) or disc (Gorti & Hollenbach 2008) contribution to the observed $[O\,I]_{63}$

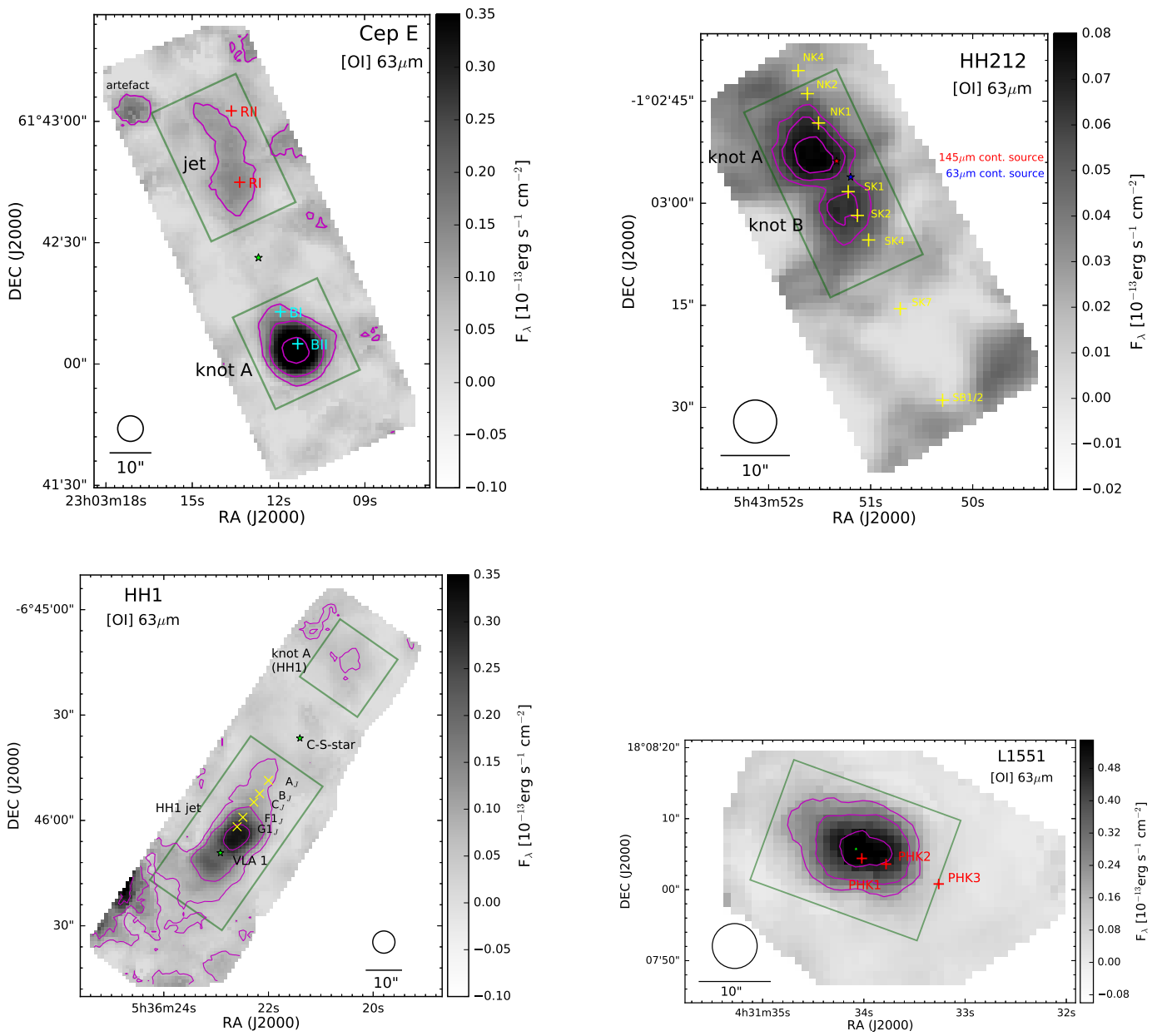

Fig. 5: Continuum-subtracted [O I]$_{63}$ maps of Cep E, HH 1, HH 212, and L1551 IRS5. The black circle shows the FWHM spatial beam size in the blue channel of the FIFI-LS instrument. The light green stars indicate the position of the respective jet-driving source. Schematic views are presented in Fig. 11 of the Appendix. Contour lines are drawn in magenta in logarithmic scale at three intensity levels (IL). **Cep E:** RI, RII, BI, and BII are the infrared knots seen in the Spitzer/IRAC band-two (4.5 µm) image of Cep E (see Gusdorf et al. (2017)). IL: $(0.10, 0.21, 0.45) \times 10^{-13}$ erg s^{-1} cm^{-2}. **HH 1:** Yellow crosses indicate the positions of a few selected optical knots (Bally et al. 2002). IL: $(0.06, 0.13, 0.28) \times 10^{-13}$ erg s^{-1} cm^{-2}. **HH 212:** Yellow crosses indicate the positions of the prominent H_2 knots (Zinnecker et al. 1998). IL: $(0.053, 0.062, 0.074) \times 10^{-13}$ erg s^{-1} cm^{-2}. **L1551:** The brightest near-infrared [Fe II] knots (PHK1, PHK2, PHK3) are marked as red crosses (Pyo et al. 2002). IL: $(0.20, 0.32, 0.50) \times 10^{-13}$ erg s^{-1} cm^{-2}.

line luminosity is negligible. If in turn a substantial amount of emission originates from PDRs or disc surfaces, mass-loss rates derived from these methods only represent upper limits. In this regard, complementary observations at other wavelengths can be insightful. One such extensive discussion can be found in the Appendix. In summary (see Table 5), the observed [O I]$_{63}$ line luminosity for Cep E and HH 1 is very likely contaminated by the presence of a PDR (strong contribution in Cep E and less strong in HH 1). Thus, their mass-loss rates represent upper limits at best.

Conceptually, the two methods put forward to estimate $\dot{M}_{\rm out}$ from the [O I]$_{63}$ line luminosity stand for two distinct perspectives of potentially the same physical situation. From the first perspective (Eq. 2), the oxygen atoms along the ejected outflow material are assumed to be collisionally excited in an almost neutral, dense, and warm enviroment. Thus, all oxygen atoms are assumed to be in neutral from. We note that shocks as a potential physical origin of the [O I]$_{63}$ line emission are not explicitly mentioned, and other physical processes such as chemical networks or cooling by other emission lines are deliberately ignored. Only the emitting oxygen atoms in the flow are put into focus, since only they contribute to the detected [O I]$_{63}$ emission.

Ultimately, the outflow geometry, which is the extent of the flow and the velocity of the flowing material, determines the amount of ejected material per unit time.
The second perspective (Eq. 3) is to explicitly attribute the $[O\,I]_{63}$ line emission to a single wind shock. In the HM89 model, the $[O\,I]_{63}$ line is also collisionally excited, but the physical setting causing the particle collisions is determined via shock physics (e.g. Rankine-Hugoniot relations). Assumptions on the shock type, shock velocities, gas densities, shock chemistry etc. are inferred, putting the shock as a whole in focus, whereby the emitting oxygen atoms are only one constituent among many. Compared to the first method, the shock model includes higher energy levels (higher than the lowest $^3P_{0,1,2}$ levels) in the atomic oxygen system and allows the presence of ionised oxygen. Line intensities from various species (molecular and atomic) are calculated in this framework and as a numerical result: a) the $[O\,I]_{63}$ line dominates the cooling in these shocks, and b) Eq. 3 holds approximately true.

4.3.1. Mass-loss rates from the $[O\,I]_{63}$ jet luminosity

We estimate mass-loss rates from jet luminosity in the $[O\,I]_{63}$ line, that is $L([O\,I]_{63})$, and specific jet parameters such as the tangential jet velocity v_t and the projected jet length θ (e.g. Dionatos et al. 2018). Sperling et al. (2020) derive the following useful relation:

$$\left(\frac{\dot{M}_{\rm out}^{\rm lum}}{M_\odot\,{\rm yr}^{-1}}\right) = (3.3-6.7)\times10^{-3}\cdot\left(\frac{v_t}{{\rm km\,s}^{-1}}\right)\left(\frac{''}{\theta}\right)\left(\frac{\rm pc}{D}\right)\left(\frac{L([O\,I]_{63})}{L_\odot}\right), \quad (2)$$

whereby v_t is the component of the jet velocity on the plane of the sky, and θ is the angular size of the jet. Equation 2 was derived assuming a range of temperatures ($T \sim 300$–8000 K) and a density equal to the critical density at these temperatures. Fundamentally, this assumption constrains the (unknown) level population in the atomic oxygen system and ultimately results in an uncertainty of a factor of ~ 10 in the derived mass-loss rates (Dionatos & Güdel 2017; Sperling et al. 2020). Mass-loss rates estimated via Eq. 2 are listed in Table 5.

4.3.2. Mass-loss rates from shock model

Alternatively, instantaneous mass-loss rates might be obtained from the $[O\,I]_{63}$ line luminosity applying the Hollenbach & McKee (1989) shock model (hereafter HM89). As one of the main results, this model predicts that the $[O\,I]_{63}$ line luminosity is proportional to the mass-loss rate in a single wind shock; that is,

$$\dot{M}_{\rm out}^{\rm shock} = 10^{-4}\,L([O\,I]_{63})/L_\odot\,M_\odot\,{\rm yr}^{-1}. \quad (3)$$

In the underlying wind shock scenario, the ejected material from the driving source of the outflow is fast enough to produce a dissociative J-shock, and the $[O\,I]_{63}$ line is the dominant coolant in the post-shock gas over a wide range of shock parameters ($n_0 \times v_{\rm shock} \leq 10^{12}$ cm^{-2} s^{-1}, n_0 pre-shock density, $v_{\rm shock}$ shock velocity). Other emission lines such as $[Si\,II]_{35}$ and $[Fe\,II]_{26}$ might even be used as proxies for the $[O\,I]_{63}$ line measuring the mass-outflow rate (Watson et al. 2016).
However, as discussed in detail by Sperling et al. (2020), it can be quite difficult to rigorously prove the applicability of Eq. 3 to specific emission regions where $[O\,I]_{63}$ is prominently detected; hence, the HM89 method is affected by large uncertainties. In addition, if the detected $[O\,I]_{63}$ emission is caused by multiple, potentially unresolved shocks, mass-loss rates derived by the HM89 method will be overestimated.

4.4. Accretion rates

Accretion rates of protostellar sources may be determined via different methods (e.g. Beltrán & de Wit 2016, and references therein). In the widely accepted scenario of magnetospheric accretion (Camenzind 1990; Bouvier et al. 2007; Hartmann et al. 2016) material flows along stellar magnetic field lines from the accretion disc onto the forming star, causing potentially detectable emission lines to appear in the spectrum (Muzerolle et al. 1998; Rigliaco et al. 2012; Antoniucci et al. 2014) or an excess of emitted UV flux (Gullbring et al. 1998; Herczeg & Hillenbrand 2008).
In this framework, the instantaneous mass accretion rate $\dot{M}_{\rm acc}$ is calculated from the accretion luminosity $L_{\rm acc}$ and additional stellar parameters such as the stellar mass $M_\star$ and the stellar radius $R_\star$. Typically, in the case of Class 0/I sources, fiducial values for their stellar parameters are inferred, since observationally based estimates using evolutionary tracks are considered unreliable (see discussion in Contreras Peña et al. 2017). The most direct measurements of $L_{\rm acc}$ may be obtained from UV spectra, which would probably fail for any of the 14 considered outflow sources, since they are highly embedded.
In order to have a comparable set of accretion rates, we followed Mottram et al. (2017) and calculated them from

$$\dot{M}_{\rm acc} = \frac{L_{\rm acc}R_\star}{GM_\star}. \quad (4)$$

Depending on the evolutionary state of the outflow source, we adopted the following values (see discussion in Mottram et al. 2017):

Class 0: $M_\star = 0.2\,M_\odot$, $R_\star = 4\,R_\odot$, $L_{\rm acc} = L_{\rm bol}$
Class I: $M_\star = 0.5\,M_\odot$, $R_\star = 4\,R_\odot$, $L_{\rm acc} = 0.5L_{\rm bol}$.

Bolometric luminosities are taken primarily from Karska et al. (2018), and if not listed therein from van Dishoeck et al. (2011). As a caveat, we note that bolometric luminosities for the considered targets often vary by a factor of few in the literature since obtaining exact measurements is challenging (e.g. Dunham et al. 2013). As a result, mass-accretion rates estimated via Eq. 4 may feature uncertainties up to one order of magnitude. The calculated values for the accretion rates are listed in Tables 5 and 6.
In the case of Cep E, we decided to estimate its accretion rate using the same approach but with different stellar parameters. The reason for this is that Cep E-mm is an intermediate-mass protostar ($M_\star \sim 2-5\,M_\odot$, e.g. Velusamy et al. 2011), thus appearing as scaled-up version of the remaining low mass protostars of our sample (see references in Frank et al. 2014; Hartmann et al. 2016). Assuming the stellar parameters for Cep E-mm to be $M_\star \sim 3\,M_\odot$ (Velusamy et al. 2011), $L_{\rm bol} \sim 80\,L_\odot$ (Froebrich et al. 2003), and $R_\star \sim 20\,R_\odot$ (Velusamy et al. 2011), and further assuming that $L_{\rm acc} \approx L_{\rm bol}$, we estimated the accretion rate via (McKee & Ostriker 2007):

$$\left(\frac{\dot{M}_{\rm acc}}{10^{-6}\,M_\odot\,{\rm yr}^{-1}}\right) \approx \frac{1}{3.1\,f_{\rm acc}}\left(\frac{0.25\,M_\odot}{M_\star}\right)\left(\frac{R_\star}{2.5\,R_\odot}\right)\left(\frac{L_{\rm acc}}{L_\odot}\right). \quad (5)$$

With $f_{\rm acc} \approx 1$ (fraction of the gravitational potential energy released by accretion), we obtain $\dot{M}_{\rm acc} \sim 1.7\times10^{-5}\,M_\odot\,{\rm yr}^{-1}$ for Cep E-mm.

5. Discussion

5.1. Other outflow components

In order to evaluate the importance of the atomic outflow component in relation to the total outflow, we compiled mass-loss rates that were estimated via other species (Table 5). Tendentiously, mass-loss rates in our sample determined via the [O I]$_{63}$ emission line are higher than values obtained from near-infrared emission lines (H_2 or [Fe II]) and lower or comparable to values obtained from sub-millimetre molecular species such as CO.

The mass-loss rate for Cep E derived from the jet geometry is about one order of magnitude lower than the measurements from low-J CO observations undertaken by Moro-Martín et al. (2001) and Lefloch et al. (2015). This points to the conclusion that the collimated CO jet analysed in both mentioned studies represents the main outflow component (not entrained material); that is, the jet is mainly molecular.

Nisini et al. (2005) estimated mass-flux rates along the HH 1 jet using near-infrared and optical emission lines. They found that amongst the considered jet components, the bulk mass loss resides in the partially ionised [Fe II] outflow and quantifies about $6\times10^{-7}\,M_\odot\,\mathrm{yr}^{-1}$ (summing over all knots). This is almost one order of magnitude lower than the mass loss determined via [O I], indicating that the bulk contribution resides in a low-excited atomic jet, as suspected by Nisini et al. (2005). Recent observations of the molecular component traced by low-J CO support this conclusion (Tanabe et al. 2019).

The mass loss residing in the molecular (in particular CO, SO, SiO) high-velocity component of the innermost part of the HH 212 jet was estimated as $\sim 10^{-6}\,M_\odot\,\mathrm{yr}^{-1}$ (Lee et al. 2007a; Podio et al. 2015; Lee et al. 2015). Surprisingly, an almost identical mass-loss rate is found in the atomic component seen in [O I]$_{63}$. Both components therefore contribute almost equally to the total mass-loss rate from the driving source.

In H_2, Davis et al. (2000) provided mass-loss rates of the order of $\sim 10^{-7}\,M_\odot\,\mathrm{yr}^{-1}$ for the inner two knots (NK1 and SK1). Therefore, even though the HH 212 jet is most prominently seen in H_2, the bulk mass of the outflow does not reside in that component of the molecular gas mixture.

With regard to L1551, the mass-loss connected to the neutral wind component is seen in the 21 cm HI line emission and was estimated as $8.6\times10^{-7}\,M_\odot\,\mathrm{yr}^{-1}$ (Giovanardi et al. 2000); that is, about the same value derived from the [O I]$_{63}$ emission. This points to the conclusion that at least parts of the neutral gas seen in the 21 cm line is cooled, entrained material due to the partially ionised wind (Pyo et al. 2002), and an unknown amount might be directly connected to the driving atomic jet seen in [O I]$_{63}$ (Giovanardi et al. 2000). From near-infrared observations, Davis et al. (2003) estimated $\dot{M}_{\mathrm{[Fe\,II]}} \sim 2\times10^{-7}\,M_\odot\,\mathrm{yr}^{-1}$ and $\dot{M}_{\mathrm{H_2}} \sim 4\times10^{-8}\,M_\odot\,\mathrm{yr}^{-1}$, indicating that the atomic component is comparably more important in transporting outflow material.

Surprisingly high outflow rates have been measured in molecular transitions of, for example, CO and are of the order of $10^{-5}\,M_\odot\,\mathrm{yr}^{-1}$ (e.g. Hogerheijde et al. 1998; Fridlund et al. 2002; Yıldız et al. 2015). That is to say they are at least a factor of 10 higher compared to the outflow rate determined here. However, this material is rather connected to entrained material, since it is has been traced by low-velocity, low-J CO emission. Conclusively, the L1551 outflow is predominantly atomic.

5.2. Efficiencies of sources with spatially resolved [O I]$_{63}$ outflows

Until now, only a handful of protostellar outflows had been mapped to a great extent in the far-infrared [O I]$_{63,145}$ emission lines. However, spatially resolving the [O I] emission from young outflow sources and analysing the spectral properties and overall morphology are crucial for drawing further conclusions on the energy budget of the outflow. High resolution maps provide valuable insights into the physical origin of the seen emission, and together with observations at other wavelengths the notion of the shock origin of the [O I] line can be supported or refuted (see e.g. discussion in Sperling et al. (2020).

The two main instruments that have been used for mapping protostellar outflows in far-infrared emission lines are SOFIA/FIFI-LS and Herschel/PACS. We compiled a set of 14 young sources (nine Class 0 and five Class I) that have been mapped along their outflow in [O I]$_{63}$. Sources observed with only one footprint of the 5×5 spaxel array of Herschel/PACS are excluded from this sample but are considered in Section 5.4.

Three additional sources from SOFIA/FIFI-LS: Sperling et al. (2020) probed five Class I/II outflows (HH 111, HH 34, SVS13 A, HH 26, and HH 30) with FIFI-LS aboard SOFIA. A detailed analysis showed that only for three of the sources (HH 111 IRS, SVS13 A, HH34 IRS) could outflow rates be determined. Seven additional sources from Herschel/PACS: Nisini et al. (2015) observed five Class 0/I sources and their outflows, namely L1448-C (Class 0), NGC 1333-IRS4 (Class 0), HH 46 (Class I), BHR 71 (Class 0), and VLA 1623 (Class 0). Dionatos et al. (2018) mapped the HH 211 protostellar system driven by HH 211-MM (Class 0) in [O I]$_{63}$ and various molecular transitions (CO, H_2O, and OH). Dionatos & Güdel (2017) mapped the NGC 1333 star forming region in [O I]$_{63}$ and [C II]$_{157}$ covering several known outflow sources such as SVS13 A, IRAS 4A, IRAS 2A S-N, SK1, and SK 14. The atomic jets connected to IRAS 4A and SVS13 A were already mapped by Nisini et al. (2015) and Sperling et al. (2020), respectively. Since the IRAS 2A S-N outflow in the Dionatos & Güdel (2017) map is clearly distinguishable from other outflows in the crowded field, we only include this source in our sample.

Given the uncertainty of the applicability of the HM89 shock model (Eq. 3), we present newly calculated mass-loss rates (with the exception of HH 34, HH 111, and SVS13 A) based on the [O I]$_{63}$ line luminosity (Eq. 2) in Table 6. With only one exception (SVS13 A), all mass-loss rates calculated via the HM89 formula are higher compared to the values from Eq. 2. This points to the conclusion that the HM89 formula indeed overestimates mass-loss rates because parts of the [O I]$_{63}$ emission are not connected to the impact of the original protostellar wind with the ambient medium. Several other internal shocks in the flow (spatially unresolved) and the presence of a PDR are the main interfering influences on the detected [O I]$_{63}$ emission. We therefore based our further analysis on mass-loss rates derived from Eq. 2.

Accretion rates of the additional outflow sources (Table 6) were calculated as described in Section 4.4. Only in the cases of HH 34 and SVS13 A are accretion-induced emission lines used as a proxy to determine their accretion luminosity and mass-accretion rates (both sources were not part of the WISH, WILL, DIGIT, or GASPS surveys). Thus, for all other sources mass-accretion rates were estimated rather indirectly and might feature high uncertainties. However, as long as further direct measurements are not yet available, the cited accretion rates in Tables 5 and 6 may be considered adequate estimates.

In this context, there is growing evidence that episodic accretion

Table 6: Mass-loss rates and accretion rates for outflow sources that have been mapped extensively in $[O\,I]_{63}$.

Source	Class	D (pc)	θ (")	v_t (km s^{-1})	$L([O\,I])$ $L_\odot$	$\dot{M}_{out}^{lum}([O\,I])$	$\dot{M}_{out}^{shock}([O\,I])$ ($10^{-7}\,M_\odot\,yr^{-1}$)	$\dot{M}_{other}$ & component	$\dot{M}_{acc}{}^a$ ($10^{-7}\,M_\odot\,yr^{-1}$)	Main ref.
HH 111 IRS	I	420	20	270	2.5×10^{-2}	26 – 53	22.9 – 26.4	4 & CO[b]	27[k]	Sperling et al. (2020)
HH 111 jet		420	45	260	1.3×10^{-2}	6 – 12	$\lesssim$ 10 – 16	2 – 6 & [O I]λ6300[r]		
SVS13A	I	235	22	270	1.5×10^{-2}	25 – 51	13.1 – 16.0	8.9 & [Fe II][c]	140 – 170[l]	Sperling et al. (2020)
								7.0 & H_2[c]		
								30 & HI[d]		
								90 & low-J CO[e] , swept-up gas		
HH 34 IRS	I	430	26	160	2.4×10^{-2}	11 – 23	20.7 – 27.5	0.7 & [Fe II][c]	35 – 115[m]	Sperling et al. (2020)
								0.03 & H_2[c]		
								$\sim$ 1.5 & [O I]λ6300[r]		
L1448-C	0	232	45	170	1.8×10^{-3}	1 – 2	2 – 4	$\sim$ 24 & SiO, SO, CO[f]	35	Nisini et al. (2015)
IRAS4A	0	235	38	100 – 140	9.1×10^{-4}	0.3 – 1.0	1 – 2	$\gtrsim$ 18 & SiO, SO, CO[g]	58	Nisini et al. (2015)
HH 46	I	450	59	300	2.0×10^{-2}	7 – 15	20 – 40	15 – 28 & CO[v]	34[n]	Nisini et al. (2015)
BHR 71	0	200	33	50 – 100	3.2×10^{-3}	1 – 3	3 – 6	21 & CO[t]	73[o]	Nisini et al. (2015)
VLA 1623	0	120	78	60	2.1×10^{-3}	0.5 – 1	2 – 4	16 – 160 & CO	21	Nisini et al. (2015)
HH 211 SE lobe	0	250	51	115	3.92×10^{-3}	1.2 – 2.4	3.9			
HH 211 NW lobe	0	250	45	115	3.57×10^{-3}	1.2 – 2.4	3.6			
HH 211 both lobes						2.4 – 4.8	7.5	7 – 28 & SiO, CO, SO[h]	14[p]	Dionatos et al. (2018)
								$\sim$ 20 – 28 & H_2[i]		
IRAS 2A, blue lobe SN	0	235	188	50	3.5×10^{-3}	0.1 – 0.3	3.5	200 & CO[u]		
IRAS 2A, red lobe SN	0	235	133	50	4.1×10^{-3}	0.2 – 0.4	4.1	400 & CO[u]		
IRAS 2A, both lobes SN						0.3 – 0.7	7.6	6 & H_2[j]	234[q]	Dionatos & Güdel (2017)
								> 6.7 & SiO, SO, CO[s]		

Notes. [a] Calculated as described in Section 4.4. [b] Lefloch et al. (2007), the high-velocity outflowing gas is detected therein in the CO J=7–6 transition. We therefore think that the stated mass-loss rate is connected to the jet itself and not to swept-up gas. [c] Davis et al. (2003). [d] Lizano et al. (1988). [e] Calculated from Knee & Sandell (2000), from Table 1 therein we adopt the relevant values for the blue lobe of HH 7-11 ($\dot{P} = \dot{M}_{out} v = 2.8\times10^{-4}\,M_\odot\,km\,s^{-1}\,yr^{-1}$, $v = 31\,km\,s^{-1}$). [f] Podio et al. (2020); Lee (2020). The stated value is in good agreement with measurements of Yoshida et al. (2021). [g] Podio et al. (2020); Yıldız et al. (2015) measure $\dot{M}_{out} > 160\times10^{-7}\,M_\odot\,yr^{-1}$ based on CO J=6–5 observations (sum of both lobes). [h] Lee et al. (2007b, 2010); Lee (2020). [i] Dionatos et al. (2010). [j] Maret et al. (2009). [k] The stated accretion rate is in good agreement with Lee (2010). Yang et al. (1997) estimate a higher value of $6.9\times10^{-6}\,M_\odot\,yr^{-1}$. [l] We estimate this accretion rate from the Brγ line (see Appendix 6). [m] Based on measurements of accretion-induced emission lines Antoniucci et al. (2008) estimate an accretion rate of $\dot{M}_{acc} \sim 41.1\times10^{-7}\,M_\odot\,yr^{-1}$, whereas Nisini et al. (2016) $\dot{M}_{acc} \sim 75\pm40\times10^{-7}\,M_\odot\,yr^{-1}$. Hartigan et al. (1994) state $\dot{M}_{acc} \sim 110\times10^{-7}\,M_\odot\,yr^{-1}$. We combine the mentioned values to a range of $(35-115)\times10^{-7}\,M_\odot\,yr^{-1}$. [n] Antoniucci et al. (2008) estimate $2.2\times10^{-7}\,M_\odot\,yr^{-1}$ based on a substantially lower bolometric luminosity. [o] Yang et al. (2017) estimate $1.2\times10^{-5}\,M_\odot\,yr^{-1}$. [p] The stated accretion rate is about a factor of six lower than the value estimated by Lee et al. (2007c), who however assume a substantially lower mass for the HH 211 protostar $M_\star = 0.06\,M_\odot$. [q] The stated value lies inbetween the values estimated by Brinch et al. (2009) and Hsieh et al. (2019), that are $94\times10^{-7}\,M_\odot\,yr^{-1}$ and $500\times10^{-7}\,M_\odot\,yr^{-1}$ respectively. [r] Hartigan et al. (1994). [s] Podio et al. (2020). [t] Yang et al. (2017); Yıldız et al. (2015) measure $76\times10^{-7}\,M_\odot\,yr^{-1}$ based on CO J=6–5 observations. [u] Based on CO J=6–5 observations (Yıldız et al. 2015). [v] The stated value is taken from Nisini et al. (2015), Yıldız et al. (2015) measure $\dot{M}_{out} \sim 200\times10^{-7}\,M_\odot\,yr^{-1}$ from CO J=6–5 observations.

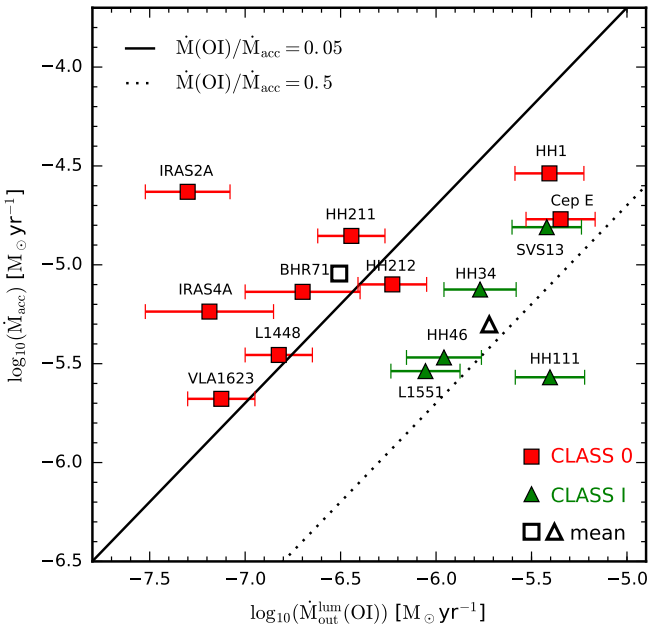

Fig. 6: $\dot{M}^{lum}_{out}$([O I]) (from Eq. 2) versus $\dot{M}_{acc}$ diagram for the extensively mapped outflow sources. The adopted mass-loss rate for Cep E is the sum of both contributions from knot A and the jet; that is, $(29.6 - 60.2) \times 10^{-7}\,M_\odot\,yr^{-1}$. In the case of HH 1, we considered the measurement at the HH 1 jet to be the best representation of the instantaneous mass-loss rate. Geometric means for Class 0/I outflows are plotted as non-filled black markers. Error bars in accretion rates are not depicted, but can be of the order of one magnitude.

and ejection may be an important factor in protostellar evolution (Audard et al. 2014). In the considered outflow sample, IRAS2A, for instance, shows a high accretion rate. IRAS2A is likely undergoing an accretion burst (Hsieh et al. 2019) potentially explaining the high accretion rate as compared to the mass-ejection rate.

Figure 6 shows the mass-loss rate $\dot{M}^{lum}_{out}$([O I]) derived from the $[O\,I]_{63}$ line luminosity as a function of the accretion rate $\dot{M}_{acc}$ for the fully mapped outflows. Half of the sources feature efficiency ratios of $\dot{M}^{lum}_{out}([O\,I])/\dot{M}_{acc} \sim 0.05 - 0.5$. This range for the outflow efficiency ratio is consistent with a) proposed jet launching models; that is, the X-wind scenario (Shu et al. 1988, 1994), or magnetohydrodynamical disc wind models (Ferreira 1997; Casse & Ferreira 2000); and b) other observational studies such as Ellerbroek et al. (2013), Mottram et al. (2017), Podio et al. (2020), Yoshida et al. (2021), and Lee (2020). Similar efficiency ratios are also found in massive protostellar outflows (e.g. Beuther et al. 2002). Since $\dot{M}^{lum}_{out}([O\,I])/\dot{M}_{acc} \lesssim 1.0$ for all our observed targets except for HH 111, we conclude that they are accretion-dominated. Geometric means of the mass-accretion rates for Class 0 and Class I outflow sources are almost the same; that is, $\sim 10^{-5}\,M_\odot\,yr^{-1}$. The geometric mean of the mass-ejection rates for the fully mapped Class 0 and Class I outflows are $3 \times 10^{-7}\,M_\odot\,yr^{-1}$ and $2 \times 10^{-6}\,M_\odot\,yr^{-1}$, respectively. In Fig. 6, Class I outflow sources are clustered rather close together, whereas the Class 0 sources are scattered over a huge region in the diagram. Class 0 outflow sources are predominantly scattered in regions of the diagram where $\dot{M}^{lum}_{out}([O\,I])/\dot{M}_{acc} \lesssim 0.05$. In contrast, Class I outflow sources tend to cluster towards higher efficiency rates of the order of 0.5.

However, the separation seen in Class 0 and Class I outflow sources in Fig. 6 might be an artefact from calculating the individual accretion rates. In fact, accretion rates attributed to Class 0 sources in Eq. 4 are per se five times higher than accretion rates from Class I outflow sources with the same bolometric luminosity. A physical explanation for the trend seen in Fig. 6 could be that the mass-ejection rates traced by $[O\,I]_{63}$ in Class 0 sources are underestimated. This conclusion is supported by an analysis of the other outflow components and their contributions to the total mass-loss rate (Section 5.3).

Given the low number of analysed outflow targets, a deep statistical cluster analysis of Fig. 6 would not be very meaningful, and in addition to that our SOFIA sample may be biased since we selected the brightest and actively accreting known Class I outflow sources. However, it would be interesting to have similar observations of Class II outflows. So far, only very few Class II outflows have been observed spatially resolving the $[O\,I]_{63}$ emission along the outflow (Podio et al. 2012). Fortunately, jets from Class II sources are usually very compact ($\sim 10 - 20''$) potentially rendering extensive mapping redundant. Additionally, for these more evolved sources a substantial amount of $[O\,I]_{63}$ emission at the driving source is expected to be connected to the formed disc and not a wind shock. Properly disentangling both contributions is challenging but necessary to determine mass-loss rates (Aresu et al. 2014).

5.3. Dominant outflow components

In Tables 5 and 6, we compare mass-loss rates derived from the $[O\,I]_{63}$ line with mass-loss rates estimated via other tracers for the fully mapped outflow sources. In seven out of nine Class 0 outflows, the bulk mass-loss resides in the molecular component. Only in two cases of Class 0 outflows is the atomic component traced by $[O\,I]_{63}$ either dominant (HH 1) or comparable (HH 212) to the molecular component.

Among the five Class I outflows, four are predominantly atomic (HH 111, HH 34, SVS13 A, L1551), and in the case of HH 46 both components contribute a comparable amount to the mass loss. In this analysis, we ignored mass losses that are likely associated with entrained material.

In fact, mass-loss rates derived from CO emission may trace entrained material. In this regard, we point out that Tables 5 and 6 contain recent mass-loss rate measurements for the molecular component at high angular resolution (Podio et al. 2020; Yang et al. 2017; Yoshida et al. 2021; Lee 2020). In detail, the stated mass-loss rates for the CO, SiO, and SO outflow components of L1448-C, IRAS 4A, BHR 71, IRAS 2A, HH 211, HH 212, and Cep E can be considered as reliable estimates. They give a more reliable determination of the molecular mass-loss rate because they can better disentangle the compact high-velocity gas in the jet and the extended entrained emission.

In comparison, Yıldız et al. (2015) utilised CO observations (CO J=3–2 and CO J=6–5) at lower angular resolution to estimate mass-loss rates. Of both CO transitions, the CO J=3–2 emission line traces entrained material, and mass-loss rates derived from it are usually a factor of ~ 100 higher than the values stated in Podio et al. (2020), Yang et al. (2017), Yoshida et al. (2021), and Lee (2020). Yıldız et al. (2015) speculated that the CO J=6–5 transition potentially traces non-entrained material and may allow more reliable estimates of mass-loss rates. However, mass-loss rates derived from the CO J=6–5 line are almost always of the same order of magnitude as mass-loss rate estimates based on the CO J=3–2 transition. We therefore think that mass-loss rates derived from CO J=6–5 observations are still heavily affected by entrained gas.

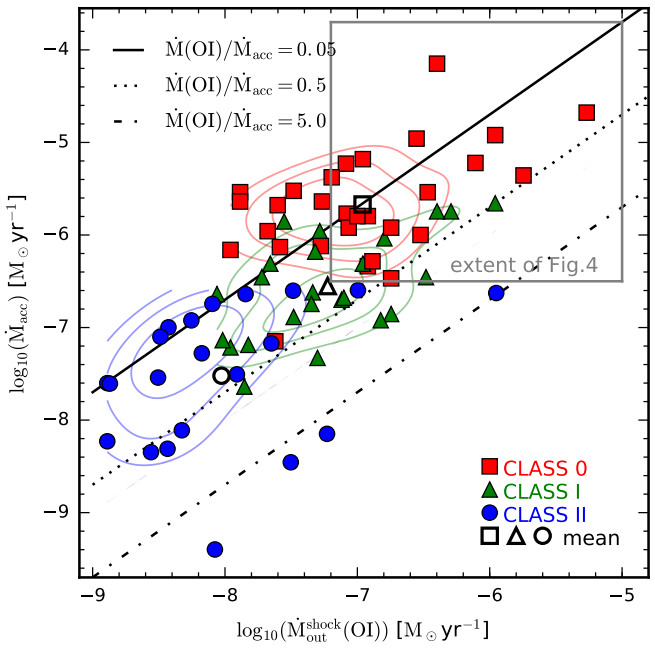

Fig. 7: Mass-loss rates $\dot{M}_{out}^{shock}$([O I]) (from Eq. 3) versus accretion rates $\dot{M}_{acc}$ of protostellar outflow sources at different evolutionary stages observed with a single Herschel/PACS footprint. Mass-outflow rates were determined assuming that the HM89 shock model conditions prevail. Geometric means for Class 0/I/II outflows are plotted as non-filled black markers. Thin coloured lines are contour lines based on a kernel-density estimate using Gaussian kernels.

In conclusion, there is evidence that the mass-loss rates of the considered Class 0 outflow sources in Fig. 6 are significantly underestimated since the molecular component contributes predominantly to the mass loss.

5.4. A comparison to sources with spatially unresolved [O I]$_{63}$ outflows

In order to compare the results from the fully mapped outflows with other studies, we compiled a list of Class 0/I/II outflow sources that have been observed with Herschel/PACS as part of the WISH+DIGIT+WILL+GASPS surveys, thus providing a single footprint with a $47'' \times 47''$ field of view in 5×5 spatial pixels of $9.4'' \times 9.4''$ each. For these outflow sources, the [O I]$_{63}$ line is either spatially unresolved or not resolved enough (e.g. the sample of Podio et al. 2012) to infer relevant properties of the jet geometry. Under the given circumstances, mass-loss rates utilising the [O I]$_{63}$ line are derived from the HM89 shock model and not from the [O I]$_{63}$ jet luminosity.

Watson et al. (2016) did a similar analysis in their survey of 84 YSOs using the Spitzer Infrared Spectrograph. Their mass-loss rate mesurements are, however, not directly based on the HM89 shock model, since the [Si II]$_{35}$ and [Fe II]$_{26}$ lines are used as a proxy for the [O I]$_{63}$ line. This introduces new uncertainties as discussed in their paper. Therefore, we do not include their sources here.

From the Herschel/PACS surveys, we selected an additional 72 outflow sources (28 Class 0, 23 Class I, and 21 Class II; see Tables 7, 8, and 9) for which the [O I]$_{63}$ line is prominently detected but mostly spatially unresolved. In detail, our selection comprises the following. Mottram et al. (2017) compiled a list of 91 protostellar sources that were observed as part of the WILL, WISH, and DIGIT surveys. From the 49 WILL sources, we only selected the 26 (15 Class 0, 11 Class I) outflow sources for which $\dot{M}_{out}$ and $\dot{M}_{acc}$ are specified in Table A.7 of that study. From the remaining 42 DIGIT+WISH sources, we excluded the sources a) for which $\dot{M}_{out}$ is not given in Table A.7; b) that were analysed in much more detail in the spatially resolved sample; c) that could not be classified fairly unambiguously as Class 0 or Class I sources. This results in 25 (13 Class 0, 12 Class I) supplementary sources. To complete our sample with even more evolved outflow sources, we included 21 Class II targets from the GASPS survey (Alonso-Martínez et al. 2017). In this study, 26 outflow sources are listed. We excluded four sources for which no accretion rates were specified or the classification was unsure. Among the selected 21 targets, the Podio et al. (2012) sample is included, with the exception of DG Tau B (TAU04 in Mottram et al. 2017). However, we took the newly determined [O I]$_{63}$ line fluxes specified in Alonso-Martínez et al. (2017) to recalculate the mass-loss rates via Eq. 3. The [O I]$_{63}$ line fluxes have changed since the Herschel/PACS data were reduced using HIPEv10 in Alonso-Martínez et al. (2017), whereas Podio et al. (2012) used HIPE 4.0.1467. For a discussion of this data reduction issue, we invite the reader to consult, for example, Howard et al. (2013). The stated accretion rates for these more evolved sources are determined from the U-band excess.

Figure 7 shows $\dot{M}_{out}^{shock}$([O I]) versus $\dot{M}_{acc}$ for the selected 72 sources. For a better comparison, we mark the coverage of the same plot for the fully mapped outflow sources (Fig. 6) as grey rectangle. Mass-loss rates $\dot{M}_{out}^{shock}$([O I]) in Figure 7 were determined via the HM89 shock model, meaning they potentially suffer from large uncertainties. From Fig. 7, four principal tendencies can be recognised: (1) Most sources are roughly located within the efficiency stripe of $f \sim 0.05 - 0.5$, which is in line with our previous findings. However, four Class I sources feature $f \gtrapprox 1.0$, and four Class II sources show even higher efficiencies $f \gtrapprox 5.0$, indicating that they are outflow-dominated. In these sources, a contribution from PDRs or discs could be more relevant; (2) Many Class 0 outflows feature conspicuously low efficiency ratios $f < 0.05$. The same trend is seen in the outflow sample of Fig. 6. For these targets, the total mass-loss rate from the [O I]$_{63}$ emission line could have been underestimated due to a significant molecular contribution. In this context, Yıldız et al. (2015) and Mottram et al. (2017) utilised CO observations to measured mass-loss rates residing in the molecular outflow component (values are listed in Tables 7 and 8). In particular, the mass-loss rates traced by CO J=6–5 in Yıldız et al. (2015) are insightful, since this gas may not be entrained material but part of the actual outflow. However, the analysis in Sect. 5.3 indicates that mass-loss rates based on CO J=6–5 observations are still substantially affected by entrained material. In this regard, observations at higher angular resolution as undertaken by Podio et al. (2020), Yang et al. (2017), Yoshida et al. (2021), and Lee (2020) may provide more robust mass-loss rate estimates. A comparison of both outflow components (atomic and molecular) is presented in Table 7. The notion that in Class 0 outflow sources the molecular component is the dominant compared to the atomic is well supported by these data. However, the comparison also shows that limitedly mapped Class I outflow sources do not necessarily feature a dominant atomic outflow component. Extensive mapping in [O I]$_{63}$ might be necessary to draw meaningful conclusions; (3) Sources from the same Class are grouping in overlapping clusters as indicated by coloured contour lines in Fig. 7, which represent a kernel-density estimate. In agreement with the findings of Ellerbroek et al. (2013) and Watson et al. (2016), there is a trend for which both mass-accretion

and mass-loss rates evolve from higher to lower values passing from Class 0 to Class II. A similar conclusion cannot be drawn from the fully mapped outflows alone, since the sample is too small and biased towards brightest outflow sources; (4) There is a broad scatter in the $\dot{M}_{\rm out}$ versus $\dot{M}_{\rm acc}$ diagram. Various factors play a role here: a) accretion rates of the younger sources might have been underestimated due to higher obscuration (Bacciotti et al. 2011); b) time variability (Watson et al. 2016); c) the [O I] emission line is exclusively used as a proxy to estimate the total instantaneous mass-loss rate. However, several other outflow components might contribute an unknown amount to the total mass-loss rate, or the underlying shock conditions might not entirely prevail (Sperling et al. 2020).

We note that Fig. 7 has some obvious shortcomings compared to Fig. 6. In Fig. 7, the mass-loss rates are purely based on the HM89 shock model. However, the applicability of the HM89 shock model has not been evaluated for any of the included sources. It is possible that for many sources in Fig. 7 the derived mass-loss rates are only of limited informative value, if the HM89 shock conditions do not prevail. In this regard, Fig. 6 is more meaningful since the $[\mathrm{O\,I}]_{63}$ jet luminosity and the individual geometric properties of the outflows are taken into account. Such a detailed analysis became possible with our new SOFIA observations, which spatially resolve the $[\mathrm{O\,I}]_{63}$ line in the extended jets. However, the comparision with other outflow contributions clearly demonstrated that $[\mathrm{O\,I}]_{63}$ maps alone are not enough to evaluate the evolution of protostellar outflows.

5.5. The role of the atomic outflow component in the evolutionary picture

There is a growing number of observational studies showing that the low-excitation, atomic outflow component traced by $[\mathrm{O\,I}]_{63}$ plays a crucial role in the overall outflow evolution (e.g. Nisini et al. 2015; Watson et al. 2016; Alonso-Martínez et al. 2017). In fact, as protostellar outflow sources evolve from Class 0 to Class II, their accretion rates and mass-loss rates tend to decrease (Watson et al. 2016), while the decisive ratio $\dot{M}_{\rm out}/\dot{M}_{\rm acc}$ may even remain constant (Podio et al. 2012). In this context, it is sometimes speculated that the mass-loss rate determined via the $[\mathrm{O\,I}]_{63}$ emission line may truly represent the bulk ejected material reflecting the anticipated outflow evolution (Dionatos & Güdel 2017). However, our observations and the comparison with other surveys suggest, as already pointed out by Nisini et al. (2015), that this hypothesis is barely true in outflows from Class 0 sources, where the bulk of ejected material resides mainly in the molecular component. Thus, for these outflows mass-loss rates determined via $[\mathrm{O\,I}]_{63}$ can be significantly underestimated. Qualitatively, these jets are largely not fast enough and too dense to be dissociative, and therefore they show very low excitation. As the source evolves towards the Class II stage, temperatures increase, densities decrease, winds become faster, and dissociative shocks connected to internal or wind shocks cause prominent atomic and ionic emission features depending on the specific excitation conditions in the flow material. These more evolved outflows become prominently detectable in, for example, [Fe II], [S II], [Si II], and [O I], effectively tracing the same gas component at low excitation. As a result, the low-excitation outflow component associated with Class I/II sources and traced by $[\mathrm{O\,I}]_{63}$ potentially (but not necessarily) represents the dominant contribution to the total mass loss. It would be interesting to see a $\dot{M}_{\rm out}$ versus $\dot{M}_{\rm acc}$ diagram that considers all relevant outflow components in order to obtain a clear picture on the importance of the mass loss traced by $[\mathrm{O\,I}]_{63}$.

It becomes clear that the importance of [O I] emission as a tracer of mass loss changes over time during the formation of the protostar, and that the far-infrared $[\mathrm{O\,I}]_{63}$ emission alone cannot be used as a sole tracer to study the evolution of $\dot{M}_{\rm out}/\dot{M}_{\rm acc}$ during the whole star formation process.

6. Summary

This paper presents SOFIA/FIFI-LS observations, that is, spectroscopic maps in the $[\mathrm{O\,I}]_{63,145}$ transitions, of four protostellar outflows associated with Cep E, HH 1, HH 212, and L1551 IRS5. For each associated continuum source, we determined flux values at 63 µm and 145 µm. Notable $[\mathrm{O\,I}]_{63}$ emission was detected in all outflow regions, however with different morphologies.

For L1551 IRS5, HH 1, and HH 212, most $[\mathrm{O\,I}]_{63}$ is detected close to their respective driving sources, whereas at Cep E-mm no $[\mathrm{O\,I}]_{63}$ is seen. A detailed analysis indicates that in the cases of L1551 IRS5 and HH 212, the Hollenbach & McKee (1989) shock conditions most likely prevail, meaning that the detected $[\mathrm{O\,I}]_{63}$ emission is connected to dissociative J-shocks. In the other cases, an unknown amount of $[\mathrm{O\,I}]_{63}$ emission can be associated to PDR regions or non-dissociative shocks.

Utilising the $[\mathrm{O\,I}]_{63}$ line luminosity (Eq. 2), we calculated mass-loss rates for Cep E, HH 1, HH 212, and L1551 that are in the range of $(5-50)\times10^{-7}\,M_{\odot}\,\mathrm{yr}^{-1}$. A comparison with mass-loss rates connected to other species showed that a) for HH 1, the bulk mass ejected from the driving source resides in the atomic [O I] component; b) the outflows associated with Cep E and L1551 are predominantly molecular; and c) the ejected mass in the HH 212 outflow is almost equally partitioned in an atomic and molecular component.

Taking accretion rates from former studies, we estimate efficiency ratios ($f = \dot{M}_{\rm out}/\dot{M}_{\rm acc}$) that are largely in the range of $f \sim 0.05-0.5$. This finding is consistent with theoretical predictions (e.g. Shu et al. (1988, 1994); Ferreira (1997); Casse & Ferreira (2000)) and other observational studies (Ellerbroek et al. 2013; Mottram et al. 2017).

We compared our findings with survey data of 72 Class 0/I/II outflow sources that have been observed in $[\mathrm{O\,I}]_{63}$ using a single Herschel footprint (5×5 spatial pixels covering a $47''\times47''$ FOV) as part of the DIGIT, WILL, WISH, and GASPS surveys. Most of these outflow sources show efficiency ratios that are consistent with our observations ($f \sim 0.05-0.5$). Surprisingly, many outflows from Class 0 sources feature low efficiency ratios: $f < 0.05$. We conclude that for Class 0 outflow sources the bulk ejected material resides in the molecular component, and mass-loss rates exclusively estimated from the $[\mathrm{O\,I}]_{63}$ emission line underestimate the total mass-loss substantially. In the case of more evolved outflows from Class I and Class II sources, the low-excitation, atomic gas component can represent the main outflow component. There is a trend of gradually decreasing accretion and mass-loss rates as sources evolve from the Class 0 to the Class II stage. However, this depicted trend needs further confirmation considering all main outflow components.

Acknowledgements. This research is based on observations made with the NASA/DLR Stratospheric Observatory for Infrared Astronomy (SOFIA). SOFIA is jointly operated by the Universities Space Research Association, Inc. (USRA), under NASA contract NNA17BF53C, and the Deutsches SOFIA Institut (DSI) under DLR contract 50 OK 0901 to the University of Stuttgart. This work has been supported by the German Verbundforschung grant 50OR1717 to JE. Teresa Giannini and Brunella Nisini acknowledge the support of the project PRIN-INAF-MAIN-STREAM 2018 *Protoplanetary disks seen through the eyes of new-generation instruments*. We thank Bill Vacca for providing us with the ATRAN-models.

References

Alcalá, J. M., Manara, C. F., Natta, A., et al. 2017, A&A, 600, A20
Alonso-Martínez, M., Riviere-Marichalar, P., Meeus, G., et al. 2017, A&A, 603, A138
AMI Consortium, Ainsworth, R. E., Scaife, A. M. M., et al. 2012, MNRAS, 423, 1089
Anderson, D. E., Bergin, E. A., Maret, S., & Wakelam, V. 2013, ApJ, 779, 141
Andre, P., Ward-Thompson, D., & Barsony, M. 1993, ApJ, 406, 122
Anglada, G., Rodríguez, L. F., & Carrasco-González, C. 2018, A&A Rev., 26, 3
Antoniucci, S., García López, R., Nisini, B., et al. 2014, A&A, 572, A62
Antoniucci, S., Nisini, B., Giannini, T., & Lorenzetti, D. 2008, A&A, 479, 503
Aresu, G., Kamp, I., Meijerink, R., et al. 2014, A&A, 566, A14
Audard, M., Ábrahám, P., Dunham, M. M., et al. 2014, in Protostars and Planets VI, ed. H. Beuther, R. S. Klessen, C. P. Dullemond, & T. Henning, 387
Ayala, S., Noriega-Crespo, A., Garnavich, P. M., et al. 2000, AJ, 120, 909
Bacciotti, F., Whelan, E. T., Alcalá, J. M., et al. 2011, ApJ, 737, L26
Bally, J. 2016, ARA&A, 54, 491
Bally, J., Feigelson, E., & Reipurth, B. 2003, ApJ, 584, 843
Bally, J., Heathcote, S., Reipurth, B., et al. 2002, AJ, 123, 2627
Bally, J., Reipurth, B., & Davis, C. J. 2007, in Protostars and Planets V, ed. B. Reipurth, D. Jewitt, & K. Keil, 215
Beltrán, M. T. & de Wit, W. J. 2016, A&A Rev., 24, 6
Bergin, E. A., Melnick, G. J., & Neufeld, D. A. 1998, ApJ, 499, 777
Beuther, H., Schilke, P., Sridharan, T. K., et al. 2002, A&A, 383, 892
Bieging, J. H. & Cohen, M. 1985, ApJ, 289, L5
Bouvier, J., Alencar, S. H. P., Boutelier, T., et al. 2007, A&A, 463, 1017
Brinch, C., Jørgensen, J. K., & Hogerheijde, M. R. 2009, A&A, 502, 199
Cabrit, S., Codella, C., Gueth, F., & Gusdorf, A. 2012, A&A, 548, L2
Cabrit, S., Codella, C., Gueth, F., et al. 2007, A&A, 468, L29
Camenzind, M. 1990, Reviews in Modern Astronomy, 3, 234
Caratti o Garatti, A., Giannini, T., Nisini, B., & Lorenzetti, D. 2006, A&A, 449, 1077
Casse, F. & Ferreira, J. 2000, A&A, 361, 1178
Chen, X., Arce, H. G., Zhang, Q., et al. 2013, ApJ, 768, 110
Chini, R., Ward-Thompson, D., Kirk, J. M., et al. 2001, A&A, 369, 155
Codella, C., Cabrit, S., Gueth, F., et al. 2007, A&A, 462, L53
Cohen, M., Harvey, P. M., & Schwartz, R. D. 1985, ApJ, 296, 633
Cohen, M. & Schwartz, R. D. 1979, ApJ, 233, L77
Colditz, S., Beckmann, S., Bryant, A., et al. 2018, Journal of Astronomical Instrumentation, 7, 1840004
Contreras Peña, C., Lucas, P. W., Kurtev, R., et al. 2017, MNRAS, 465, 3039
Davis, C. J., Cervantes, B., Nisini, B., et al. 2011a, A&A, 528, A3
Davis, C. J., Cervantes, B., Nisini, B., et al. 2011b, A&A, 528, A3
Davis, C. J., Smith, M. D., & Eislöffel, J. 2000, MNRAS, 318, 747
Davis, C. J., Stern, L., Ray, T. P., & Chrysostomou, A. 2002, A&A, 382, 1021
Davis, C. J., Whelan, E., Ray, T. P., & Chrysostomou, A. 2003, A&A, 397, 693
Devine, D., Reipurth, B., & Bally, J. 1997, in IAU Symposium, Vol. 182, Herbig-Haro Flows and the Birth of Stars, ed. B. Reipurth & C. Bertout, 91
Devine, D., Reipurth, B., & Bally, J. 1999, AJ, 118, 972
Dionatos, O. & Güdel, M. 2017, A&A, 597, A64
Dionatos, O., Nisini, B., Cabrit, S., Kristensen, L., & Pineau Des Forêts, G. 2010, A&A, 521, A7
Dionatos, O., Ray, T., & Güdel, M. 2018, A&A, 616, A84
Dunham, M. M., Arce, H. G., Allen, L. E., et al. 2013, AJ, 145, 94
Eislöffel, J., Mundt, R., & Bohm, K.-H. 1994, AJ, 108, 1042
Eislöffel, J., Smith, M. D., Davis, C. J., & Ray, T. P. 1996, AJ, 112, 2086
Ellerbroek, L. E., Podio, L., Kaper, L., et al. 2013, A&A, 551, A5
Feeney-Johansson, A., Purser, S. J. D., Ray, T. P., et al. 2019, ApJ, 885, L7
Ferreira, J. 1997, A&A, 319, 340
Fischer, C., Beckmann, S., Bryant, A., et al. 2018, Journal of Astronomical Instrumentation, 7, 1840003
Fischer, W. J., Megeath, S. T., Ali, B., et al. 2010, A&A, 518, L122
Flower, D. R. & Pineau Des Forêts, G. 2010, MNRAS, 406, 1745
Flower, D. R., Pineau des Forets, G., Field, D., & May, P. W. 1996, MNRAS, 280, 447
Frank, A., Ray, T. P., Cabrit, S., et al. 2014, Protostars and Planets VI, 451
Fridlund, C. V. M., Bergman, P., White, G. J., Pilbratt, G. L., & Tauber, J. A. 2002, A&A, 382, 573
Fridlund, C. V. M. & Liseau, R. 1994, A&A, 292, 631
Fridlund, C. V. M. & Liseau, R. 1998, ApJ, 499, L75
Fridlund, C. V. M., Liseau, R., Djupvik, A. A., et al. 2005, A&A, 436, 983
Froebrich, D. 2005, ApJS, 156, 169
Froebrich, D., Smith, M. D., Hodapp, K. W., & Eislöffel, J. 2003, MNRAS, 346, 163
Galván-Madrid, R., Avila, R., & Rodríguez, L. F. 2004, Rev. Mexicana Astron. Astrofis., 40, 31
Giannini, T., Nisini, B., & Lorenzetti, D. 2001, ApJ, 555, 40
Gibb, A. G., Richer, J. S., Chandler, C. J., & Davis, C. J. 2004, ApJ, 603, 198
Giovanardi, C., Rodríguez, L. F., Lizano, S., & Cantó, J. 2000, ApJ, 538, 728
Goldsmith, P. F. 2019, ApJ, 887, 54
Gómez-Ruiz, A. I., Gusdorf, A., Leurini, S., et al. 2012, A&A, 542, L9
Gorti, U. & Hollenbach, D. 2008, ApJ, 683, 287
Gramajo, L. V., Whitney, B. A., Kenyon, S. J., Gómez, M., & Merrill, K. M. 2007, AJ, 133, 1911
Green, J. D., Evans, II, N. J., Jørgensen, J. K., et al. 2013, ApJ, 770, 123
Greene, T. P., Wilking, B. A., Andre, P., Young, E. T., & Lada, C. J. 1994, ApJ, 434, 614
Gueth, F. & Guilloteau, S. 1999, A&A, 343, 571
Gullbring, E., Hartmann, L., Briceño, C., & Calvet, N. 1998, ApJ, 492, 323
Gusdorf, A., Anderl, S., Lefloch, B., et al. 2017, A&A, 602, A8
Hartigan, P., Frank, A., Foster, J. M., et al. 2011, ApJ, 736, 29
Hartigan, P., Holcomb, R., & Frank, A. 2019, ApJ, 876, 147
Hartigan, P., Morse, J., Palunas, P., Bally, J., & Devine, D. 2000, AJ, 119, 1872
Hartigan, P., Morse, J. A., & Raymond, J. 1994, ApJ, 436, 125
Hartmann, L., Calvet, N., Gullbring, E., & D'Alessio, P. 1998, ApJ, 495, 385
Hartmann, L., Herczeg, G., & Calvet, N. 2016, ARA&A, 54, 135
Hayashi, M. & Pyo, T.-S. 2009, ApJ, 694, 582
Herczeg, G. J. & Hillenbrand, L. A. 2008, ApJ, 681, 594
Hester, J. J., Stapelfeldt, K. R., & Scowen, P. A. 1998, AJ, 116, 372
Hogerheijde, M. R., van Dishoeck, E. F., Blake, G. A., & van Langevelde, H. J. 1998, ApJ, 502, 315
Hollenbach, D. & McKee, C. F. 1989, ApJ, 342, 306
Howard, C. D., Sandell, G., Vacca, W. D., et al. 2013, ApJ, 776, 21
Hsieh, T.-H., Murillo, N. M., Belloche, A., et al. 2019, ApJ, 884, 149
Itoh, Y., Kaifu, N., Hayashi, M., et al. 2000, PASJ, 52, 81
Karska, A., Herczeg, G. J., van Dishoeck, E. F., et al. 2013, A&A, 552, A141
Karska, A., Kaufman, M. J., Kristensen, L. E., et al. 2018, ApJS, 235, 30
Kaufman, M. J. & Neufeld, D. A. 1996, ApJ, 456, 611
Knee, L. B. G. & Sandell, G. 2000, A&A, 361, 671
Kun, M., Kiss, Z. T., & Balog, Z. 2008, Star Forming Regions in Cepheus, ed. B. Reipurth, Vol. 4, 136
Lada, C. J. 1987, in IAU Symposium, Vol. 115, Star Forming Regions, ed. M. Peimbert & J. Jugaku, 1–17
Ladd, E. F. & Hodapp, K. W. 1997, ApJ, 474, 749
Lee, C.-F. 2010, ApJ, 725, 712
Lee, C.-F. 2020, A&A Rev., 28, 1
Lee, C.-F., Hasegawa, T. I., Hirano, N., et al. 2010, ApJ, 713, 731
Lee, C.-F., Hirano, N., Zhang, Q., et al. 2014, ApJ, 786, 114
Lee, C.-F., Hirano, N., Zhang, Q., et al. 2015, ApJ, 805, 186
Lee, C.-F., Ho, P. T. P., Beuther, H., et al. 2006, ApJ, 639, 292
Lee, C.-F., Ho, P. T. P., Hirano, N., et al. 2007a, ApJ, 659, 499
Lee, C.-F., Ho, P. T. P., Palau, A., et al. 2007b, ApJ, 670, 1188
Lee, C.-F., Ho, P. T. P., Palau, A., et al. 2007c, ApJ, 670, 1188
Lee, C.-F., Li, Z.-Y., Codella, C., et al. 2018, ApJ, 856, 14
Lee, C.-F., Mundy, L. G., Reipurth, B., Ostriker, E. C., & Stone, J. M. 2000, ApJ, 542, 925
Lefloch, B., Cernicharo, J., Pacheco, S., & Ceccarelli, C. 2011, A&A, 527, L3
Lefloch, B., Cernicharo, J., Reipurth, B., Pardo, J. R., & Neri, R. 2007, ApJ, 658, 498
Lefloch, B., Eislöffel, J., & Lazareff, B. 1996, A&A, 313, L17
Lefloch, B., Gusdorf, A., Codella, C., et al. 2015, A&A, 581, A4
Lim, J. & Takakuwa, S. 2006, ApJ, 653, 425
Liseau, R., Fridlund, C. V. M., & Larsson, B. 2005, ApJ, 619, 959
Lizano, S., Heiles, C., Rodriguez, L. F., et al. 1988, ApJ, 328, 763
Looney, L. W., Geis, N., Genzel, R., et al. 2000, in Proc. SPIE, Vol. 4014, Airborne Telescope Systems, ed. R. K. Melugin & H.-P. Röser, 14–22
Looney, L. W., Mundy, L. G., & Welch, W. J. 1997, ApJ, 484, L157
Lord, S. D. 1992, A new software tool for computing Earth's atmospheric transmission of near- and far-infrared radiation, Tech. rep.
Maret, S., Bergin, E. A., Neufeld, D. A., et al. 2009, ApJ, 698, 1244
McCaughrean, M., Zinnecker, H., Andersen, M., Meeus, G., & Lodieu, N. 2002, The Messenger, 109, 28
McKee, C. F. & Ostriker, E. C. 2007, ARA&A, 45, 565
Mighell, K. J. 1999, in Astronomical Society of the Pacific Conference Series, Vol. 189, Precision CCD Photometry, ed. E. R. Craine, D. L. Crawford, & R. A. Tucker, 50
Molinari, S. & Noriega-Crespo, A. 2002, AJ, 123, 2010
Moro-Martín, A., Noriega-Crespo, A., Molinari, S., et al. 2001, ApJ, 555, 146
Mottram, J. C., van Dishoeck, E. F., Kristensen, L. E., et al. 2017, A&A, 600, A99
Muzerolle, J., Hartmann, L., & Calvet, N. 1998, AJ, 116, 2965
Neckel, T. & Staude, H. J. 1987, ApJ, 322, L27
Nisini, B., Bacciotti, F., Giannini, T., et al. 2005, A&A, 441, 159
Nisini, B., Codella, C., Giannini, T., et al. 2007, A&A, 462, 163
Nisini, B., Giannini, T., Antoniucci, S., et al. 2016, A&A, 595, A76
Nisini, B., Giannini, T., & Lorenzetti, D. 2002, ApJ, 574, 246
Nisini, B., Santangelo, G., Giannini, T., et al. 2015, ApJ, 801, 121

Noriega-Crespo, A. 2002, in Revista Mexicana de Astronomia y Astrofisica Conference Series, Vol. 13, Revista Mexicana de Astronomia y Astrofisica Conference Series, ed. W. J. Henney, W. Steffen, L. Binette, & A. Raga, 71–78
Noriega-Crespo, A., Garnavich, P. M., & Molinari, S. 1998, AJ, 116, 1388
Noriega-Crespo, A. & Raga, A. C. 2012, ApJ, 750, 101
Noriega-Crespo, A., Raga, A. C., Lora, V., & Rodríguez-Ramírez, J. C. 2020, Rev. Mexicana Astron. Astrofis., 56, 29
Noriega-Crespo, A., Raga, A. C., Moro-Martín, A., Flagey, N., & Carey, S. J. 2014, New Journal of Physics, 16, 105008
Osorio, M., D'Alessio, P., Muzerolle, J., Calvet, N., & Hartmann, L. 2003, ApJ, 586, 1148
Ospina-Zamudio, J., Lefloch, B., Ceccarelli, C., et al. 2018, A&A, 618, A145
Ospina-Zamudio, J., Lefloch, B., Favre, C., et al. 2019, MNRAS, 490, 2679
Podio, L., Codella, C., Gueth, F., et al. 2015, A&A, 581, A85
Podio, L., Kamp, I., Flower, D., et al. 2012, A&A, 545, A44
Podio, L., Tabone, B., Codella, C., et al. 2020, arXiv e-prints, arXiv:2012.15379
Pravdo, S. H., Rodriguez, L. F., Curiel, S., et al. 1985, ApJ, 293, L35
Pyo, T.-S., Hayashi, M., Kobayashi, N., et al. 2002, ApJ, 570, 724
Pyo, T.-S., Hayashi, M., Kobayashi, N., Terada, H., & Tokunaga, A. T. 2009, ApJ, 694, 654
Raga, A. C., Reipurth, B., Cantó, J., Sierra-Flores, M. M., & Guzmán, M. V. 2011, Rev. Mexicana Astron. Astrofis., 47, 425
Ray, T. P., Mundt, R., Dyson, J. E., Falle, S. A. E. G., & Raga, A. C. 1996, ApJ, 468, L103
Reipurth, B., Davis, C. J., Bally, J., et al. 2019, AJ, 158, 107
Reipurth, B., Heathcote, S., Yu, K. C., Bally, J., & Rodríguez, L. F. 2000, ApJ, 534, 317
Rieke, G. H. & Lebofsky, M. J. 1985, ApJ, 288, 618
Rigliaco, E., Natta, A., Testi, L., et al. 2012, A&A, 548, A56
Rodríguez, L. F., Canto, J., Torrelles, J. M., & Ho, P. T. P. 1986, ApJ, 301, L25
Rodríguez, L. F., D'Alessio, P., Wilner, D. J., et al. 1998, Nature, 395, 355
Rodríguez, L. F., Delgado-Arellano, V. G., Gómez, Y., et al. 2000, AJ, 119, 882
Rodríguez, L. F., Porras, A., Claussen, M. J., et al. 2003, ApJ, 586, L137
Shu, F., Najita, J., Ostriker, E., et al. 1994, ApJ, 429, 781
Shu, F. H., Lizano, S., Ruden, S. P., & Najita, J. 1988, ApJ, 328, L19
Smith, M. D., Khanzadyan, T., & Davis, C. J. 2003, MNRAS, 339, 524
Smith, M. D., O'Connell, B., & Davis, C. J. 2007, A&A, 466, 565
Sperling, T., Eislöffel, J., Fischer, C., et al. 2020, Probing the hidden atomic gas in Class I jets with SOFIA
Stocke, J. T., Hartigan, P. M., Strom, S. E., et al. 1988, ApJS, 68, 229
Strom, K. M., Strom, S. E., & Vrba, F. J. 1976, AJ, 81, 308
Tafalla, M. 2013, in Astronomical Society of the Pacific Conference Series, Vol. 476, New Trends in Radio Astronomy in the ALMA Era: The 30th Anniversary of Nobeyama Radio Observatory, ed. R. Kawabe, N. Kuno, & S. Yamamoto, 177
Tafalla, M., Liseau, R., Nisini, B., et al. 2013, A&A, 551, A116
Takakuwa, S., Saigo, K., Matsumoto, T., et al. 2020, ApJ, 898, 10
Takami, M., Chrysostomou, A., Ray, T. P., et al. 2006, ApJ, 641, 357
Tanabe, Y., Nakamura, F., Tsukagoshi, T., et al. 2019, PASJ, 71, S8
van Dishoeck, E. F., Kristensen, L. E., Benz, A. O., et al. 2011, PASP, 123, 138
Velusamy, T., Langer, W. D., Kumar, M. S. N., & Grave, J. M. C. 2011, ApJ, 741, 60
Vig, S., Veena, V. S., Mandal, S., Tej, A., & Ghosh, S. K. 2018, MNRAS, 474, 3808
Watson, D. M., Calvet, N. P., Fischer, W. J., et al. 2016, ApJ, 828, 52
White, G. J., Liseau, R., Men'shchikov, A. B., et al. 2000, A&A, 364, 741
White, R. J. & Hillenbrand, L. A. 2004, ApJ, 616, 998
Yang, J., Ohashi, N., Yan, J., et al. 1997, ApJ, 475, 683
Yang, Y.-L., Evans, Neal J., I., Green, J. D., Dunham, M. M., & Jørgensen, J. K. 2017, ApJ, 835, 259
Yang, Y.-L., Green, J. D., Evans, Neal J., I., et al. 2018, ApJ, 860, 174
Yıldız, U. A., Kristensen, L. E., van Dishoeck, E. F., et al. 2015, A&A, 576, A109
Yoshida, T., Hsieh, T.-H., Hirano, N., & Aso, Y. 2021, ApJ, 906, 112
Young, E. T., Becklin, E. E., Marcum, P. M., et al. 2012, ApJ, 749, L17
Zinnecker, H., McCaughrean, M. J., & Rayner, J. 1996, HH 212: The Most Beautiful Protostellar Jet Known to Date, ed. S. Beckwith, J. Staude, A. Quetz, & A. Natta, Vol. 465, 572
Zinnecker, H., McCaughrean, M. J., & Rayner, J. T. 1998, Nature, 394, 862
Zucker, C., Speagle, J. S., Schlafly, E. F., et al. 2019, arXiv e-prints [arXiv:1902.01425]

Appendix A: Continuum maps

The obtained continuum maps of Cep E, HH 1, HH 212, and L1551 at the two wavelengths 63.18 µm ($\Delta\lambda$ = 0.3 µm) and 145.53 µm ($\Delta\lambda$ = 1.0 µm) are shown in Fig. 8 (bandwidths are in parentheses). Continuum flux measurements are presented in Table 3.

Appendix B: [O I]$_{145}$ map of HH 212

We present the continuum-subtracted [O I]$_{145}$ map of HH 212 in Fig. 9. A bright emission feature (knot C), very likely shocked material, is detected in a region not covered by the corresponding [O I]$_{63}$ map. A sample spaxel from that specific region at the [O I]$_{145}$ transition is shown in Fig. 10.

Appendix C: Estimate of the SVS13A accretion rate

The accretion rate of SVS13A can be estimated via the emission in the Brγ line at $\lambda = 2.166$ µm. Davis et al. (2011a) measured a line flux of $F^{\rm obs}_{\rm Br\gamma} = (249 \pm 5) \times 10^{-17}$ W m^{-2}. We corrected this line flux assuming the extinction law (Rieke & Lebofsky 1985):

$$A_\lambda / A_{\rm v} = (\lambda_{\rm v}/\lambda)^{1.6}\,, \tag{6}$$

and

$$F^0_{\rm Br\gamma} = F^{\rm obs}_{\rm Br\gamma} \times 10^{A_\lambda/2.5}, \tag{7}$$

whereby $A_{\rm v}$ represents the visual extinction at $\lambda_{\rm v} = 0.55$ µm and $F^0_{\rm Br\gamma}$ is the extinction-corrected line flux. We assume $A_{\rm v} = 10$ (Davis et al. 2011b). Thus, at $D = 235$ pc, we obtain a line luminosity of $L({\rm Br}\gamma) \approx 1.2 \times 10^{-2}\,L_\odot$. Therefore, the accretion luminosity estimated via

$$\log(L_{\rm acc}/L_\odot) = a \times \log(L({\rm Br}\gamma)/L_\odot) + b,$$

with $a = 1.19 \pm 0.10$, and $b = 4.02 \pm 0.51$ (Alcalá et al. 2017) is $L_{\rm acc} \approx 54\,L_\odot$. This value is consistent with the bolometric luminosity stated in Davis et al. (2011b); that is, $L_{\rm bol} = 50 - 80\,L_\odot$. Inferring the fiducial values of the protostellar mass and radius of $M_\star = 0.5\,M_\odot$ and $R_\star = 4\,R_\odot$ respectively, we calculated a mass accretion rate of (Gullbring et al. 1998)

$$\dot{M}_{\rm acc} = \frac{L_{\rm acc} R_\star}{G M_\star} \approx 1.4 \times 10^{-5}\,M_\odot\,{\rm yr}^{-1}.$$

The accretion rate might be even higher by a factor of $(1 - R_\star/R_i)^{-1}$. In consideration of $R_i = 5\,R_\star$, the corresponding mass accretion rate is $\dot{M}_{\rm acc} = 1.7 \times 10^{-5}\,M_\odot\,{\rm yr}^{-1}$.

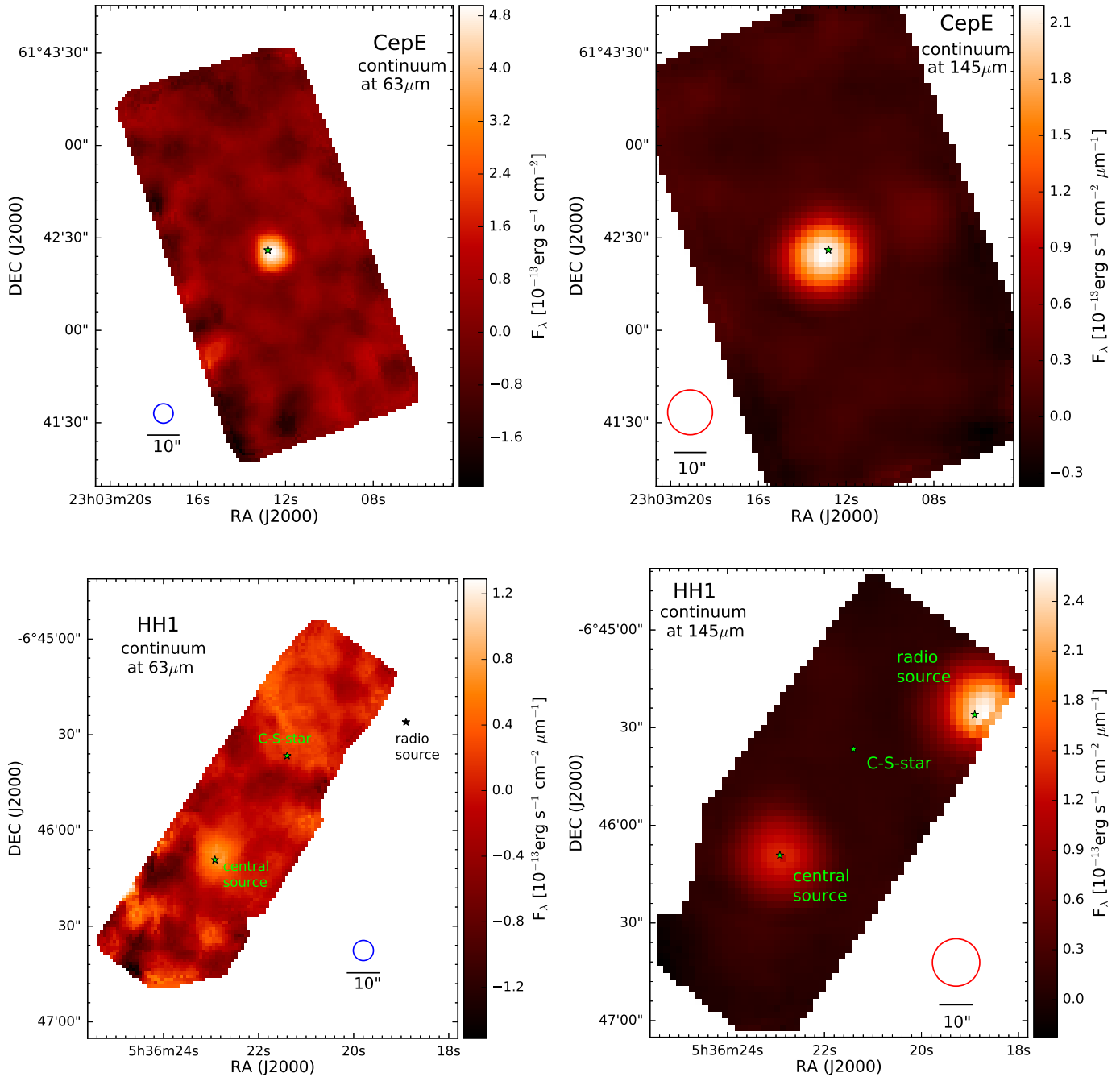

Fig. 8: Continuum maps of Cep E, HH 1, HH 212, and L1551 obtained from SOFIA/FIFI-LS observations in the two FIFI-LS channels at 63.18 µm and 145.53 µm. Green stars mark the positions of the continuum sources taken from the 2MASS catalogue (Table 1), with the exeption of HH 212. In the case of HH 212, the green stars indicate the position of the centroid of the fitted 2D Gaussian (see discussion in Section 4.1).

Appendix D: Inspecting the [O I] origin – a schematic view

In this section, we discuss the possible physical origin of the detected $[O\,I]_{63}$ emission towards the observed protostellar outflows. Associated mass-loss rates might be determined from the $[O\,I]_{63}$ line luminosity if the bulk of the detected $[O\,I]_{63}$ line emission is collisionally excited in shocks. Previous observations at other transitions may prove useful to test this crucial assumption. All schematics are shown in Fig. 11.

Cep E: The brightest $[O\,I]_{63}$ emission region knot A coincides with the Herbig-Haro object HH 377 located in the southern lobe of the Cep E outflow (Devine et al. 1997). HH 377 is a compact knot, detected prominently in [S II] and less bright in Hα indicating the presence of a weak bow-shock region. No optical [O III] or [N II] line was detected at HH 377, and therefore it must be a low-excitation object (Ayala et al. 2000). The presence of a J-shock at the apex of the HH 377 bow shock can be justified, since it is also very bright in near-infrared H_2 (e.g. Eislöffel et al. 1996; Noriega-Crespo et al. 1998). In

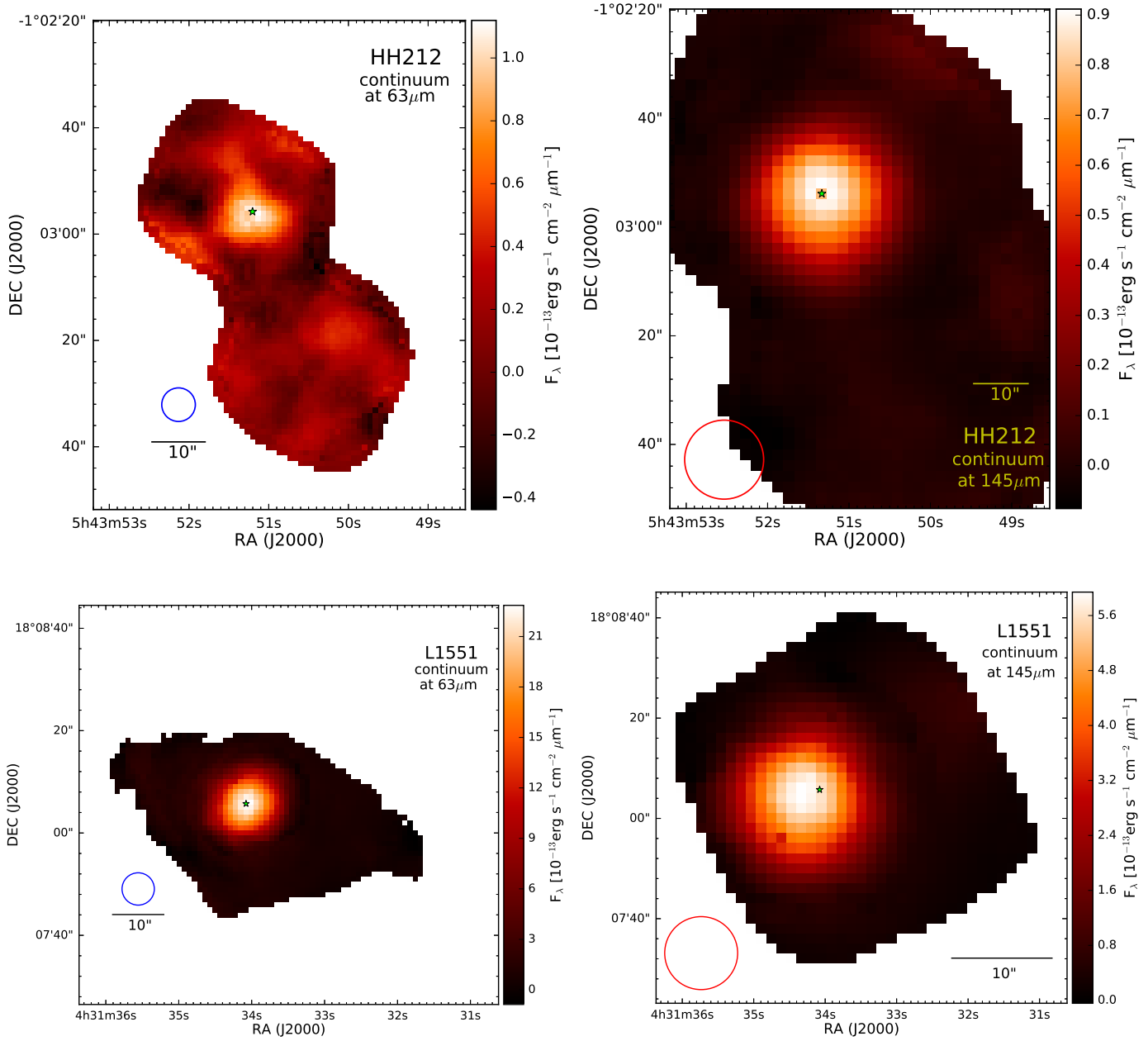

Fig. 8: Continued.

this scenario, the luminous H_2 emission at HH 377 may be attributed to C-shocks in bow-shock wings (Smith et al. 2003), and the optical emission arises from J-shocks at a potentially present Mach disc (Ayala et al. 2000; Moro-Martín et al. 2001). Therefore, the observed [O I]$_{63}$ line emission is most likely excited via collisions in a J-shock (Noriega-Crespo 2002). Since almost no near-infrared [Fe II] was detected at HH 377 (Eislöffel et al. 1996), we conclude that the shocks are predominantly non-dissociative (see discussion in e.g. Bally et al. 2007). The very faint near-infrared [Fe II] emission at HH 377 might hint at a partly dissociative reverse shock region, that is, the Mach disc. On the other hand, the [O I]$_{63}$ line is the dominant far-infrared coolant in both lobes supporting its connection to dissociative J-shocks (Giannini et al. 2001).

However, the [C II]$_{158}$/[O I]$_{63}$ line ratios at the northern and southern lobes of Cep E are of the order of $\sim$ 1 (Moro-Martín et al. 2001; Giannini et al. 2001; Smith et al. 2003), indicating that some fraction of the observed [O I]$_{63}$ emission is not connected to shocks. Moro-Martín et al. (2001) estimated that about 20 % of the observed [O I]$_{63}$ emission (in both lobes) comes from the presence of a PDR region, and 90 – 95 % of the residual [O I]$_{63}$ shock component is due to a J-shock. UV illumination by the driving protostar was discussed in Gusdorf et al. (2017).

Fortunately, the Cep E outflow could be fully mapped at the 1670 GHz (179.5 μm) H_2O emission in the Herschel-WISH survey (Tafalla et al. 2013). From our maps, we see that far from the source [O I] peaks where H_2O and H_2 peak. Additionally, a few OH lines in the far-infrared spectral range are detected towards the southern and the northern lobes (Moro-Martín et al. 2001). Therefore, we conclude that water is copiously formed at the shocked regions (knot A, jet region). Hence, the

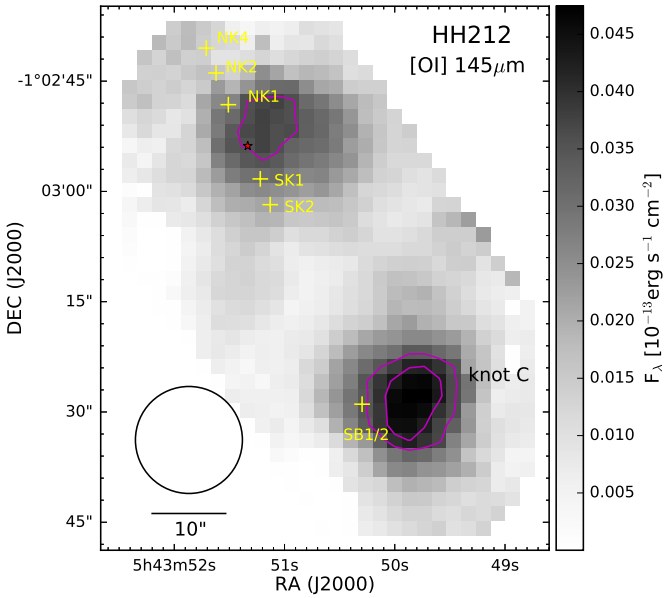

Fig. 9: The continuum-subtracted [O I]$_{145}$ emission map of HH 212. The bright emission knot C is not seen in the [O I]$_{63}$ map, since it lies outside the mapped region (see Fig.10 for the [O I]$_{145}$ line detection).

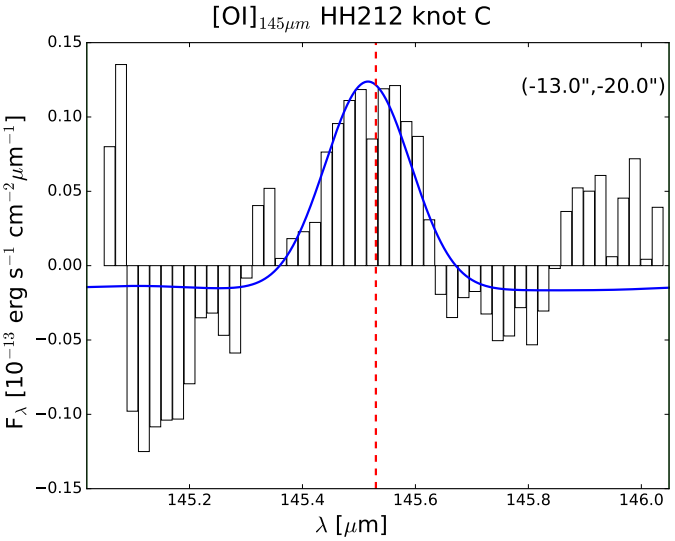

Fig. 10: Detected [O I]$_{145}$ line at knot C towards HH 212.

outflow shock reaches temperatures higher than about 400 K (low-velocity shock) leading to a chemical conversion of oxygen atoms into H_2O by their reaction with H_2 (e.g. Kaufman & Neufeld 1996; Bergin et al. 1998; Giannini et al. 2001; Flower & Pineau Des Forêts 2010; Tafalla 2013).

At the driving source, Cep E mm, we detect no [O I]$_{63,145}$. In fact, the lack of emission at other emission lines such as H_2, [Fe II], and Hα towards Cep E mm points to the conclusion that it must be an extremely deeply embedded source (Ladd & Hodapp 1997) or system of two sources (Moro-Martín et al. 2001; Ospina-Zamudio et al. 2018). Close to Cep E mm, Lefloch et al. (2011) and Ospina-Zamudio et al. (2018) detected a bipolar SiO emission along the north-south flow. This emission roughly matches with the H_2O emission (see also Tafalla 2013), indicating the presence of low-velocity C-shocks potentially interacting with dust grains (e.g. Flower et al. 1996; Nisini et al. 2007).

An outflow cavity is seen in CO (Lefloch et al. 2015) which is in line with the schematic view of the southern outflow lobe of Cep E presented in Moro-Martín et al. (2001). Ospina-Zamudio et al. (2019) detected hot, dense knots along the almost symmetric CO-jet that can be attributed to internal jet shocks. However, an atomic jet component towards knot A is not seen in our maps, indicating that the jet is mainly molecular (Ospina-Zamudio et al. 2019). The perpendicular, small-scale outflow discovered by Eislöffel et al. (1996) in H_2 is not detected in our maps, but it is potentially connected to the second SiO flow detected by Ospina-Zamudio et al. (2018). We suspect that it is either too faint to be detected in our study or unfavourable shock conditions prevail (e.g. small shock regions, a mainly molecular jet, high extinction). In CO, Ladd & Hodapp (1997) report another, but large-scale (fossil), outflow that is not seen in our [O I] maps either.

At the spatial resolution of our maps, the northern redshifted lobe of the Cep E outflow is detected in [O I] as one jet-like structure. The same region reveals a highly complex and knotty internal structure seen prominently in H_2 (Ladd & Hodapp 1997). No optical Hα, [S II], or near-infrared [Fe II] is detected there. Therefore, we conclude that this region is associated with multiple, primarily non-dissociative bow shocks. Velusamy et al. (2011) identified three consecutive bow shocks along the flow at the northern emission region. In [O I], only one of them is present at the outermost tip of the emission region.

The [O I] emission is slightly curved towards the east and matches the H_2 emission in the lower part of the region. Further upstream curvatures on [O I] and H_2 differ slightly, indicating that both emissions arise from different environments. Eislöffel et al. (1996) proposed that a precession of the outflow is responsible for the wiggling structure seen in H_2. In this context, it seems interesting that in [O I] a different wiggle curvature is seen. Considering that the wiggling of the jet was observed 23 years ago, the different wiggle morphology can be interpreted as a temporal evolution of the precessing jet. Alternatively, deflection regions along the jet axis - in particular at the tip of the northern bow shock - mimic precession of the outflow source.

Fortunately, the [O I]$_{145}$ line is detected in the Cep E jet region (signal-to-noise ratio ~ 3), yielding a line ratio of [O I]$_{63}$/[O I]$_{145}$ ~ 23 in perfect agreement with Giannini et al. (2001). A similar ratio was found in the Cep E blue lobe (Giannini et al. 2001). Depending on pre-shock densities and shock velocities, the Hollenbach & McKee (1989) shock model predicts [O I] line ratios to be between 10 and 35, which is consistent with our measurement. From the collision diagram presented in Nisini et al. (2015), we measure collider densities of $n \sim 10^{4.3} - 10^{5.4}$ cm^{-3}.

HH 1: Most detected [O I]$_{63}$ coincides with the location of the well-studied optical HH 1 jet and its associated chain of shock-excited emission knots (e.g. Hester et al. 1998; Bally et al. 2002; Hartigan et al. 2011). As in the optical, the [O I]$_{63}$ emission fades out about 30″ downstream of the driving source VLA1. Naturally, the HH 1 jet is interpreted as collimated outflow featuring a series of internal shocks with bow-shock morphology (e.g. Ray et al. 1996). We therefore conclude that the bulk of the observed [O I]$_{63}$ emission is connected to the HH 1 jet, its shocks, and its associated internal working surfaces. The detected [O I]$_{63}$ emission south-east of VLA1 can be attributed to the counter jet (Noriega-Crespo & Raga 2012). Interestingly, in [O I]$_{63}$ only one very bright clumpy knot about 5″ north-west of VLA1 is seen roughly coinciding with the innermost optical knot G1$_J$ and the two bright knots of HH 501

(Hester et al. 1998). So, it may be the case that only one shock region, such as a strong disc wind or a few shock-excited knots are responsible for the main [O I]$_{63}$ emission at the HH 1 jet base. In this context, it is worth mentioning that VLA 1 is a highly obscured source, so the lack of [O I]$_{63}$ emission - and near-infrared [Fe II], H_2 emission - at the jet base might be attributed to the dense molecular envelope (Davis et al. 2000; Reipurth et al. 2000).

Furthermore, towards VLA 1 and HH 1 line ratios of [O I]$_{63}$/[C II]$_{157}$,$\sim$ 1-2 were measured, indicating that a substantial amount of the observed [O I]$_{63}$ emission (about 50 %) may not originate from shocks but from the impact of PDR regions (Giannini et al. 2001; Molinari & Noriega-Crespo 2002). However, at VLA 1 and HH 1, far-infrared line ratios of [O I]$_{63}$/[O I]$_{145}$ $\sim$ 30 and [O I]$_{63}$/[O I]$_{145}$ $\sim$ 25 (Giannini et al. 2001; Molinari & Noriega-Crespo 2002) are consistent with predictions from the Hollenbach & McKee (1989) J-shock model. Nevertheless, the presence of C-shocks cannot be ruled out from that finding alone (Giannini et al. 2001). More importantly, the [O I]$_{63}$ dominates the far-infrared line cooling in both regions, which can indirectly be interpreted as a confirmation of the assumption that the bulk [O I]$_{63}$ emission originates from a dissociative J-shock (Giannini et al. 2001). Indeed, dissociative shock signatures are certified, since near-infrared [Fe II] emission about 3″ north-west of VLA1 is prominently detected (Davis et al. 2000).

We detect some clumpy [O I]$_{63}$ emission about 65″ north-west of VLA1, that is, at the location of the feature-rich HH 1 complex. In the optical, HH 1 is prominently seen in Hα, [S II], and [O III], indicating the presence of multiple bow shocks, internal emission knots, filametary structures, and an extended cooling zone (e.g. Hartigan et al. 2011). The [O I]$_{63}$ emission is mostly seen behind the leading bow shocks, and therefore this emission is likely connected to the cooling zone behind dissociative shocks.

HH 212: The highly symmetric HH 212 outflow with a projected size of about 240″ ($\sim$ 0.5 pc) is most prominently seen in molecular transitions; that is, in H_2 (e.g. Zinnecker et al. 1998; McCaughrean et al. 2002; Smith et al. 2007), SiO (e.g. Codella et al. 2007; Lee et al. 2007a; Cabrit et al. 2007), or CO (e.g. Gueth & Guilloteau 1999; Lee et al. 2000, 2006). Surprisingly, no optical counterpart of the innermost part of the jet has been detected in Hα and [S II] (Reipurth et al. 2019), indicating that the jet's nature might be mainly molecular (Zinnecker et al. 1996) or that high extinction prevents such a detection in the optical. Nevertheless, the atomic component of the HH 212 jet seen in our [O I]$_{63}$ maps can be traced back to the driving source, IRAS 05413–0104, and consolidates the presence of strong shocks in a dense environment (Gibb et al. 2004; Takami et al. 2006). The detected [O I]$_{63}$ emission matches the mid-infrared [Fe II]$_{26}$ and [S I]$_{25}$ emission very well (Anderson et al. 2013), supporting the notion of dissociative J-shocks and slow C-shocks being present at NK1 and SK1 (Hollenbach & McKee 1989; Kaufman & Neufeld 1996). Furthermore, Caratti o Garatti et al. (2006) and Smith et al. (2007) detected strong near-infrared [Fe II] emission at both of these knots, supporting the dissociative J-shock assumption. A potential bow-shock morphology featuring a Mach disc at NK1 and SK1 is unresolved in our maps. Strong disc wind signatures have been detected at the driving source (Lee et al. 2018). Thus, some of the detected [O I]$_{63}$ emission might be connected to this disc wind.

Further downstream in both lobes, that is, towards knots SK2 and NK2 and beyond, the [O I] emission rapidly faints out, indicating that only at NK1 and SK1 are the shocks strong enough to excite [O I]$_{63}$ (Lee et al. 2007a). At the other knots not seen in [O I], non-dissociative shocks are present. Since we detect strong [O I]$_{145}$ emission in front of SB1/2 - a region not fully mapped here in [O I]$_{63}$ - we suspect strong [O I]$_{63}$ emission to be detected there as well, indicating another dissociative J-shock region.

L1551 IRS5: In the case of L1551 IRS5, only the innermost arcmin was observed in [O I]$_{63}$, although this source is connected to multiple spectacular Herbig-Haro objects (e.g. Devine et al. 1999; Hayashi & Pyo 2009). White et al. (2000) obtained an infrared spectrum towards IRS5 (ISO LWS, beamsize $\sim$ 80″), indicating that the observed [O I]$_{63}$ line originates mainly from shocks and not a PDR region ([O I]$_{63}$/[C II]$_{157}$ $\sim$ 7.3).

The two continuum sources associated with L1551 IRS5 are embedded in a large-scale dusty envelope (Looney et al. 1997; Rodríguez et al. 1998; Fridlund et al. 2002; Takakuwa et al. 2020), and each source features a circumstellar disc, from which [O I]$_{63}$ emission can potentially originate.

From L1551 IRS5 a prominent optical jet (HH 154, Fridlund & Liseau 1998) emerges featuring a knotty internal structure, underpining the assumption of their shock origin (e.g. Fridlund & Liseau 1994; Hartigan et al. 2000; Fridlund et al. 2005). Deep optical observations proved that there are actually two westwards-directed jets at the location of HH 154, that is, the fast northern and slow southern jets (Hartigan et al. 2000).

Indeed, most of the (blueshifted) [O I]$_{63}$ emission arises between IRS 5 VLA and PHK2, meaning it is connected to the 5″ outset of the northern jet. This part of the jet is prominently seen in the near-infrared [Fe II] lines (Itoh et al. 2000; Pyo et al. 2002), H_α and [S II] (Fridlund et al. 2005), indicating that the detected [O I] emission is most likely connected to dissociative shocks in the outflow. This conclusion is supported by the noted alignment of the [O I]$_{63}$ emission at P.A.$\sim$ 250^o , which is consistent with the stated P.A. $\sim$ 260^o for the northern jet (Pyo et al. 2009). Pyo et al. (2002) recognised two velocity components in the northern [Fe II] jet of which the high-velocity ($v_{\rm LSR}$ $\sim$ $-300\,{\rm km\,s^{-1}}$) component potentially originates from a collimated stellar jet, whereas the low-velocity ($v_{\rm LSR}$ $\sim$ $-100\,{\rm km\,s^{-1}}$) component is connected to a disc wind. The observed spectral [O I]$_{63}$ line shifts in both lobes correspond to radial velocities as high as $v_{\rm rad}$ $\sim$ $100-150\,{\rm km\,s^{-1}}$, which is consistent with measurements in Lee et al. (2014), and therefore it is more likely to originate from disc winds.

The knot PHK2 is peculiar since the northern [Fe II] outflow changes direction at this location (Pyo et al. 2009). Thus, at PHK2 a deflection shock might be present causing parts of the detected [O I]$_{63}$ emission.

The brightest optical emission knot, i.e. knot D in Neckel & Staude (1987) or knot 3 in Stocke et al. (1988), is located about 10″ southwest of the source, and it is interpreted as terminal bow shock of the L1551 IRS5 jet with a Mach disc (Hartigan et al. 2000; Fridlund et al. 2005). This knot is prominently seen in Hα, [S II] (e.g. Fridlund et al 1994, Fridlund et al 2005) and coincides with the near-infrared [Fe II] knot PHK3 (Pyo et al. 2002). Surprisingly, at the position of this prominent emission knot we detect almost no [O I]$_{63}$. However, the detection of the optical [O III] line only at knot 3 (Cohen et al. 1985) hints at the presence of a strong shock (e.g. Hartigan et al. 2000; Fridlund et al. 2005) ionising almost the whole medium behind a high-velocity shock. Fridlund & Liseau (1998) estimated an extremely high ionisation fraction close to 100 % at this knot. We therefore conclude that at PHK3 a strong bow shock from HH 154 ionises almost all oxygen atoms, leaving no neutral

oxygen atoms to take part in the cooling in the cooling zone.
A very faint counter jet northeast of IRS 5 was first detected in [Fe II] by Hayashi & Pyo (2009). Since there are some spaxels at this location showing a redshifted $[O\,I]_{63}$ line, we conclude that this small-scale counter jet is tentatively detected in our maps as well. The observed $[O\,I]_{63}$ emission seems to follow the [Fe II] emission, indicating that both lines are connected to the outflow and their shocks.
At L1551 IRS 5, very weak H_2O and OH emission are detected (e.g. Tafalla 2013), indicating a complete photodissociation of these molecules (Lee et al. 2014). Herschel/PACS observations indicate that dissociative J-shocks connected to disc winds and/or both jets are responsible for the observed low water emission (Lee et al. 2014). However, C-shocks attributed to cavity shocks might also be present (Lee et al. 2014). At L1551 IRS 5, line ratios of $[O\,I]_{63}/[O\,I]_{145} \sim 10 - 20$ have been determined (Lee et al. 2014) and are in line with predictions from the (Hollenbach & McKee 1989) shock model.
In conclusion, the HM89 shock conditions very probably prevail at L1551 IRS5 and near to the HH 212 driving source (Table 4). For Cep E and HH 1, a significant (and still unknown) amount of $[O\,I]_{63}$ is connected to a PDR region, as well as to non-dissociative J-shocks.

Appendix E: Table of all objects

Tables 7–9 list 72 protostellar outflow sources that have been observed in the $[O\,I]_{63}$ transition with a single footprint with Herschel/PACS; that is, a field of view of 5×5 spatial pixels, extending $47'' \times 47''$. Thus, these observations feature limited mapping compared to the presented SOFIA data. We compared their jet efficiencies $\dot{M}_{\rm out}/\dot{M}_{\rm acc}$ with the ones determined in this study.

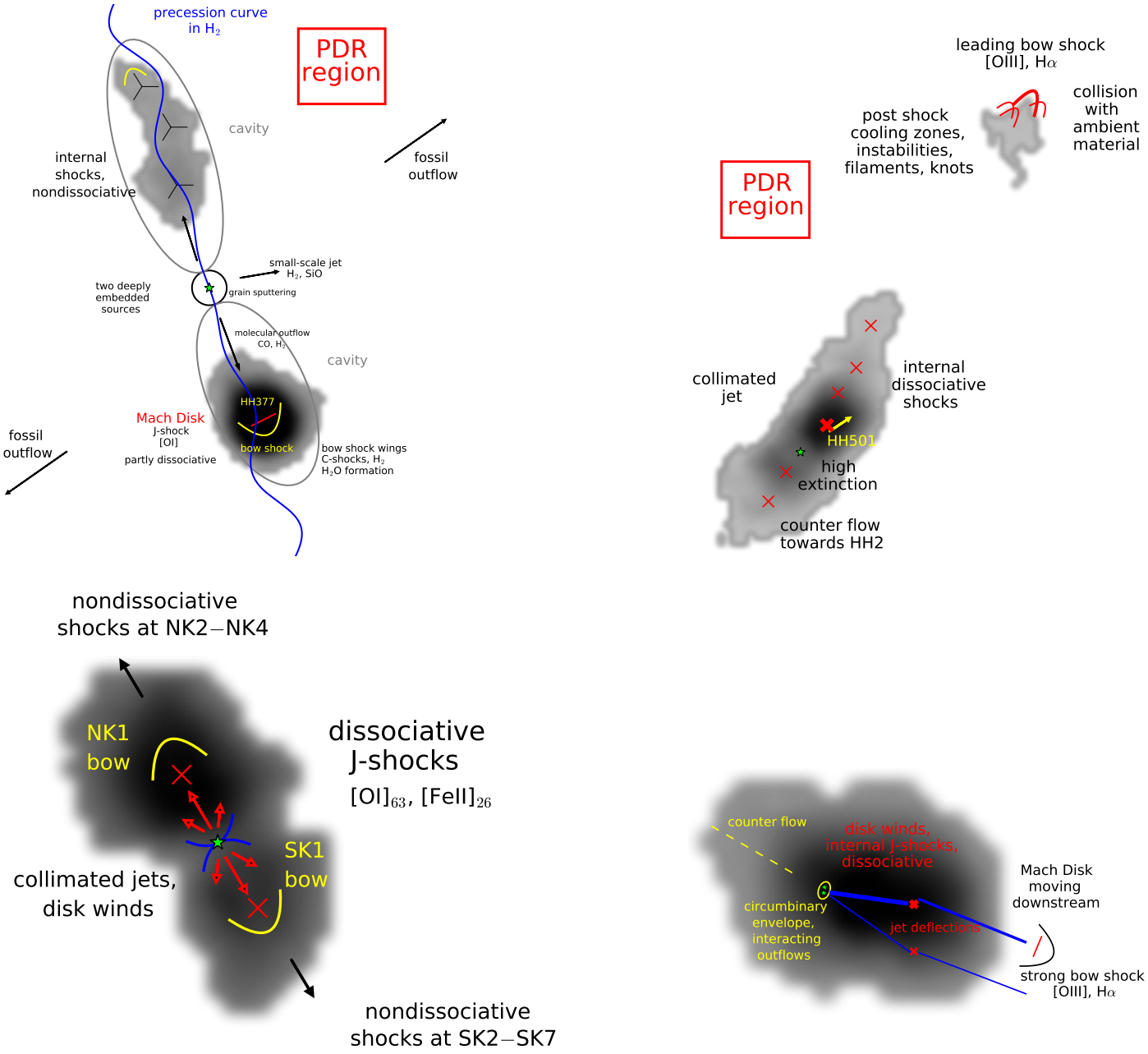

Fig. 11: Schematics of the Cep E (*upper left*), HH 1 (*upper right*), HH 212 (*lower left*), and L1551 IRS5 (*lower right*) outflow. The continuum-subtracted $[O\,I]_{63}$ emission maps from the SOFIA/FIFI-LS observations are plotted in a grey colour scale. Source positions are marked as green stars. Our interpretations of the observed $[O\,I]_{63}$ emission are based on previous studies briefly discussed in Appendix D.

Table 7: Source sample from the DIGIT and WISH surveys. We took 25 sources (13 Class 0 and 12 Class I) from Table A.7 in Mottram et al. (2017), hereafter abbreviated as Mo17, with the following selection criteria: a) $\dot{M}_{\rm acc}$ and $\dot{M}_{\rm out}$ are given in Table A.7; b) sources are not part of the spatially resolved Nisini et al. (2015) sample, which were analysed in much more detail; c) flat sources are excluded (IRAS03301+3111, IRAS12496, RNO91); d) we excluded RCRA IRS5A, RCrA-I7A, and RCrA-I7B since they are ambiguously classified.

Source	Cloud	Class[a]	RA(J2000)[b]	DEC(J2000)[b]	D	$\dot{M}_{\rm out}$([O I])	$\dot{M}_{\rm out}$(mol)	$\frac{\dot{M}_{\rm out}([\rm O\,I])}{\dot{M}_{\rm out}(\rm mol)}$ [i]	$\dot{M}_{\rm acc}$[g]	Main Ref.
			(h m s)	(° ′ ″)	(pc)	($M_\odot$ yr^{-1})	($M_\odot$ yr^{-1})		($M_\odot$ yr^{-1})	
IRAS03245+3002	Per	0	03 27 39.09	+30 13 03.0	235	6.4×10^{-8}			4.2×10^{-6}	Mo17
L1455-ISR3	Per	I	03 28 00.40	+30 08 01.3	235	5.0×10^{-8}			4.7×10^{-8}	Mo17
NGC 1333-IRAS 4B	Per	0	03 29 12.04	+31 13 01.5	235	1.3×10^{-8}	$\sim 3.5\times10^{-7}$[k]	3.7×10^{-2}	2.9×10^{-6}	Mo17
B1a	Per	I	03 33 16.66	31 07 55.2	235	1.9×10^{-8}			3.5×10^{-7}	Mo17
L1489	Tau	I	04 04 42.9	+26 18 56.3	140	2.2×10^{-8}	$\sim 6.1\times10^{-7}$[e]	3.6×10^{-2}	4.9×10^{-7}	Mo17
TMR1	Tau	I	04 39 13.9	+25 53 20.6	140	1.1×10^{-7}	$\sim 4.1\times10^{-7}$[e]	2.6×10^{-1}	4.9×10^{-7}	Mo17
TMC1A	Tau	I	04 39 35.0	+25 41 45.5	140	3.3×10^{-7}	$\sim 7.3\times10^{-7}$[e]	4.5×10^{-1}	3.5×10^{-7}	Mo17
L1527	Tau	0	04 39 53.9	+26 03 09.8	140	1.8×10^{-7}	$\sim 4.5\times10^{-6}$[e]	4.0×10^{-2}	1.2×10^{-6}	Mo17
TMC1	Tau	I	04 41 12.7	+25 46 35.9	140	1.5×10^{-7}	$\sim 1.6\times10^{-6}$[e]	9.4×10^{-2}	1.2×10^{-7}	Mo17
IRAM04191+1522	Tau	0	04 21 56.9	+15 29 45.9	140	2.4×10^{-8}			7.1×10^{-8}	Mo17
Ced110-IRS4	ChaI	0	11 06 47.0	−77 22 32.4	150	1.3×10^{-7}	$\sim 3.3\times10^{-7}$[e]	3.4×10^{-1}	5.2×10^{-7}	Mo17
IRAS15398-3359	Lup	0	15 43 01.29	−34 09 15.4	130[c]	3.0×10^{-7}	$\sim 3.2\times10^{-6}$[e]	9.4×10^{-2}	1.0×10^{-6}	Mo17
GSS30 IRS1	Oph	I	16 26 21.48	−24 23 04.2	125	5.1×10^{-7}	$\sim 1.3\times10^{-5}$[e]	3.9×10^{-3}	1.8×10^{-6}	Mo17
WL12	Oph	I	16 26 44.2	−24 34 48.4	125	7.9×10^{-8}			2.1×10^{-7}	Mo17
Elias29	Oph	I	16 27 09.36	−24 37 18.4	125	4.0×10^{-7}	$\sim 1.6\times10^{-6}$[e]	2.5×10^{-1}	1.8×10^{-6}	Mo17
IRS44	Oph	I	16 27 28.1	−24 39 33.4	125	4.8×10^{-8}			6.6×10^{-7}	Mo17
IRS46	Oph	I	16 27 29.4	−24 39 16.1	125	1.5×10^{-8}			6.5×10^{-8}	Mo17
IRS63	Oph	I	16 31 35.76	−24 01 29.2	125	3.3×10^{-8}	$\sim 1.3\times10^{-5}$[f]		1.3×10^{-7}	Mo17
L483 MM	Aqu	0	18 17 29.9	−04 39 39.5	200[c]	1.1×10^{-7}	$\sim 1.1\times10^{-5}$[e]	1.0×10^{-2}	6.6×10^{-6}	Mo17
Ser-SMM1	Ser	0	18 29 49.56	+01 15 21.9	436	4.0×10^{-7}	$\sim 2.2\times10^{-5}$[e]	1.8×10^{-2}	7.1×10^{-5}	Mo17
Ser-SMM4	Ser	0	18 29 56.7	+01 13 17.2	436	1.8×10^{-6}	$\sim 2.6\times10^{-5}$[e]	6.9×10^{-2}	4.4×10^{-6}	Mo17
Ser-SMM3	Ser	0	18 29 59.3	+01 14 01.7	436	1.1×10^{-6}	$\sim 3.9\times10^{-5}$[e]	2.8×10^{-2}	1.2×10^{-5}	Mo17
L723 MM	Core	0	19 17 53.7	+19 12 20.0	300[c]	1.3×10^{-8}	$\sim 1.5\times10^{-5}$[e]	8.7×10^{-4}	2.3×10^{-6}	Mo17
B335	Core	0	19 37 00.9	+07 34 09.6	106[d]	2.5×10^{-8}	$\sim 1.0\times10^{-7}$[j]	2.5×10^{-1}	2.1×10^{-6}	Mo17
L1157	Core	0	20 39 06.3	+68 02 16.0	325[d]	3.3×10^{-8}	$\sim 4.5\times10^{-7}$[k]	7.3×10^{-2}	3.0×10^{-6}	Mo17

Notes. [a] Classification from Nisini et al. (2002), Green et al. (2013), Karska et al. (2013), and Yang et al. (2018). [b] Coordinates from Karska et al. (2013). [c] Karska et al. (2013). [d] Green et al. (2013). [e] Yıldız et al. (2015) from CO J=6–5 observations; the listed values are the sum of the mass-loss rates of both lobes. [f] Tanabe et al. (2019) from CO J=1–0 observations, i.e. rather entrained material. [g] From Mottram et al. (2017) we adopt their method calculating the mass-accretion rates listed in Tables 5 and 6. [h] Yıldız et al. (2015) from CO J=3–2 observations; the listed values are the sum of the mass-loss rates of both lobes. As stated therein, CO J=3–2 traces entrained material. [i] Ratio of column 7 and 8, not calculated in cases where the swept-up material is traced by CO. [j] Lee (2020). [k] Podio et al. (2020).

Table 8: Source sample from the WILL survey. We only took the 26 (15 Class 0 and 11 Class I) outflow sources, for which $\dot{M}_{\rm acc}$ is presented in Table A.7 in Mo17.

Source[a]	Cloud	Class	RA(J2000)	DEC(J2000)	D	$\dot{M}_{\rm out}([\mathrm{O\,I}]_{63})$	$\dot{M}_{\rm out}$(mol)[b]	$\dot{M}_{\rm acc}$[c]	Main Ref.
			(h m s)	(° ′ ″)	(pc)	($M_\odot$ yr^{-1})	($M_\odot$ yr^{-1})	($M_\odot$ yr^{-1})	
AQU 01	Aqu	0	18 29 03.82	−01 39 01.5	436	8.3×10^{-8}	8.5×10^{-5}	1.7×10^{-6}	Mo17
AQU 02	Aqu	0	18 29 08.60	−01 30 42.8	436	8.2×10^{-8}	1.3×10^{-5}	5.9×10^{-6}	Mo17
CRA 01	CrA	0	19 02 58.67	−37 07 35.9	130	1.2×10^{-7}	2.3×10^{-6}	1.6×10^{-6}	Mo17
OPH 02	Oph	I	16 32 00.99	−24 56 42.6	125	5.2×10^{-8}	2.5×10^{-8}	1.1×10^{-6}	Mo17
PER 01	Per	0	03 25 22.32	+30 45 13.9	235	3.4×10^{-7}	8.1×10^{-5}	2.9×10^{-6}	Mo17
PER 02	Per	0	03 25 36.49	+30 45 22.2	235	7.8×10^{-7}	–	6.0×10^{-6}	Mo17
PER 04	Per	0	03 26 37.47	+30 15 28.1	235	5.3×10^{-8}	7.1×10^{-7}	7.6×10^{-7}	Mo17
PER 05	Per	I	03 28 37.09	+31 13 30.8	235	2.8×10^{-8}	1.2×10^{-7}	1.4×10^{-6}	Mo17
PER 06	Per	I	03 28 57.36	+31 14 15.9	235	1.6×10^{-7}	–	9.2×10^{-7}	Mo17
PER 07	Per	0	03 29 00.55	+31 12 00.8	235	1.2×10^{-7}	3.8×10^{-6}	4.6×10^{-7}	Mo17
PER 08	Per	I	03 29 01.56	+31 20 20.6	235	1.1×10^{-6}	1.4×10^{-5}	2.2×10^{-6}	Mo17
PER 14	Per	I	03 30 15.14	+30 23 49.4	235	4.6×10^{-8}	3.7×10^{-6}	2.4×10^{-7}	Mo17
PER 15	Per	0	03 31 20.98	+30 45 30.1	235	2.1×10^{-8}	2.4×10^{-6}	1.1×10^{-6}	Mo17
PER 16	Per	0	03 32 17.96	+30 49 47.5	235	2.6×10^{-8}	7.6×10^{-6}	7.4×10^{-7}	Mo17
PER 17	Per	I	03 33 14.38	+31 07 10.9	235	1.4×10^{-8}	1.5×10^{-5}	2.3×10^{-8}	Mo17
PER 18	Per	0	03 33 16.44	+31 06 52.5	235	1.8×10^{-7}	3.4×10^{-6}	3.4×10^{-7}	Mo17
PER 19	Per	I	03 33 27.29	+31 07 10.2	235	1.8×10^{-7}	1.7×10^{-6}	1.4×10^{-7}	Mo17
PER 21	Per	0	03 43 56.84	+32 03 04.7	235	8.6×10^{-8}	7.8×10^{-6}	1.2×10^{-6}	Mo17
PER 22	Per	0	03 44 43.96	+32 01 36.2	235	1.0×10^{-7}	1.5×10^{-6}	1.6×10^{-6}	Mo17
SERS 01	Serp	0	18 29 37.70	−01 50 57.8	436	2.8×10^{-7}	1.8×10^{-5}	1.1×10^{-5}	Mo17
TAU 01	Tau	I	04 19 58.40	+27 09 57.0	140	7.6×10^{-8}	1.7×10^{-6}	2.0×10^{-7}	Mo17
TAU 02	Tau	I	04 21 11.40	+27 01 09.0	140	1.1×10^{-8}	2.1×10^{-7}	6.1×10^{-8}	Mo17
TAU 04	Tau	I	04 27 02.60	+26 05 30.0	140	4.5×10^{-8}	7.1×10^{-7}	1.8×10^{-7}	Mo17
TAU 06	Tau	I	04 27 57.30	+26 19 18.0	140	9.6×10^{-9}	1.8×10^{-7}	7.3×10^{-8}	Mo17
W40 02	W40	0	18 31 10.36	−02 03 50.4	436	5.4×10^{-6}	1.0×10^{-5}	2.1×10^{-5}	Mo17
W40 07	W40	0	18 32 13.36	−01 57 29.6	436	5.4×10^{-8}	6.5×10^{-6}	2.3×10^{-6}	Mo17

Notes. [(a)] Source names adopted from Mottram et al. (2017). [(b)] Calculated via the same method presented in Yıldız et al. (2015) but based on low-J CO observations; that is, CO J=3–2 measuring the entrained material. [(c)] From Mottram et al. (2017), we adopted their method calculating the mass-accretion rates listed in Tables 5 and 6.

Table 9: Source sample from Alonso-Martínez et al. (2017), hereafter abbreviated as AM17. Sources were selected with the following selection criteria: a) Class II outflow sources (see Table 2 in Howard et al. 2013); b) $\dot{M}_{\rm acc}$ is given in Table A.1 in AM17; c) integrated $[\mathrm{O\,I}]_{63}$ line fluxes over 3×3 spaxels are stated with error margins in Table C.3.

Source	Cloud	Class	RA(J2000)[a]	DEC(J2000)[a]	D	$\dot{M}_{\rm out}([\mathrm{O\,I}]_{63})$	$\dot{M}_{\rm acc}$[g]	Main Ref.
			(h m s)	(° ′ ″)	(pc)	($M_\odot$ yr^{-1})	($M_\odot$ yr^{-1})	
AA Tau	Tau	II	04 34 55.42	+24 28 53.16	140	$1.29 \pm 0.37 \times 10^{-9}$[b]	2.51×10^{-8}	AM17
CW Tau	Tau	II	04 14 17.00	+28 10 57.80	140	$6.68 \pm 1.72 \times 10^{-9}$[b]	5.27×10^{-8}	AM17
DF Tau	Tau	II	04 27 03.08	+25 42 23.30	140	$3.74 \pm 0.37 \times 10^{-9}$[d]	10.05×10^{-8}	AM17
DG Tau	Tau	II	04 27 04.70	+26 06 16.30	140	$1.01 \pm 0.04 \times 10^{-7}$[b]	2.53×10^{-7}	AM17
DL Tau	Tau	II	04 33 39.06	+25 20 38.23	140	$1.35 \pm 0.12 \times 10^{-9}$[d]	2.48×10^{-8}	AM17
DO Tau	Tau	II	04 38 28.58	+26 10 49.44	140	$1.23 \pm 0.29 \times 10^{-8}$[b]	3.12×10^{-8}	AM17
DP Tau	Tau	II	04 42 37.70	+25 15 37.50	140	$8.39 \pm 1.23 \times 10^{-9}$[b]	0.04×10^{-8}	AM17
DQ Tau	Tau	II	04 46 53.05	+17 00 00.20	140	$1.29 \pm 0.25 \times 10^{-9}$[d]	0.59×10^{-8}	AM17
FS Tau	Tau	II	04 22 02.18	+26 57 30.50	140	$3.27 \pm 0.12 \times 10^{-8}$[b]	$(2-3) \times 10^{-7}$[c]	AM17
GG Tau	Tau	II	04 32 30.35	+17 31 40.60	140	$3.25 \pm 0.74 \times 10^{-9}$[b]	7.95×10^{-8}	AM17
Haro 6-13	Tau	II	04 32 15.41	+24 28 59.70	140	$3.12 \pm 0.86 \times 10^{-9}$[b]	2.88×10^{-8}[e]	AM17
HL Tau	Tau	II	04 31 38.44	+18 13 57.65	140	$3.14 \pm 0.03 \times 10^{-8}$[d]	0.35×10^{-8}	AM17
HN Tau	Tau	II	04 33 39.35	+17 51 52.37	140	$3.68 \pm 0.55 \times 10^{-9}$[b]	0.49×10^{-8}	AM17
IRAS04385+2550[f]	Tau	II	04 41 38.82	+25 56 26.75	140	$4.72 \pm 0.74 \times 10^{-9}$[b]	7.76×10^{-9}[e]	AM17
RW Aur	Tau	II	05 07 49.54	+30 24 05.07	140	$1.43 \pm 0.28 \times 10^{-8}$[b]	$(0.034-1.6) \times 10^{-6}$[c]	AM17
SU Aur	Tau	II	04 55 59.38	+30 34 01.56	140	$8.03 \pm 0.74 \times 10^{-9}$[b]	18.03×10^{-8}	AM17
T Tau	Tau	II	04 21 59.43	+19 32 06.37	140	$1.12 \pm 0.02 \times 10^{-6}$[b]	2.36×10^{-7}	AM17
UY Aur	Tau	II	04 51 47.38	+30 47 13.50	140	$2.24 \pm 0.09 \times 10^{-8}$[b]	6.74×10^{-8}	AM17
UZ Tau	Tau	II	04 32 42.89	+25 52 32.60	140	$2.76 \pm 0.86 \times 10^{-9}$[d]	0.45×10^{-8}	AM17
V773 Tau	Tau	II	04 14 12.92	+28 12 12.45	140	$5.57 \pm 0.74 \times 10^{-9}$[b]	11.95×10^{-8}	AM17
XZ Tau	Tau	II	04 31 39.48	+18 13 55.70	140	$5.90 \pm 0.36 \times 10^{-8}$[b]	0.71×10^{-8}	AM17

Notes. [a] Coordinates from Howard et al. (2013). [b] Calculated via Eq. 3 from the given line $[\mathrm{O\,I}]_{63}$ fluxes stated in Table C.3 in AM17. [c] Accretion rates from Podio et al. (2012). [d] Calculated via Eq. 3 from the given line $[\mathrm{O\,I}]_{63}$ fluxes stated in Table 1 in Aresu et al. (2014). [e] White & Hillenbrand (2004). [f] Other name: Haro 6-33. [g] Accretion rates are calculated from the U-band excess (see description in Alonso-Martínez et al. 2017).